ORNL/TM-2021/2121

# Mechanical Properties of Additively Manufactured 316L Stainless Steel Before and After Neutron Irradiation: FY21


T. S. Byun
D. A. Collins
A. G. Le Coq
T. G. Lach
K. D. Linton
M. N. Gussev
J. W. Werden
M. R. McAlister
X. Chen
C. B. Joslin
J. K. Carver
F. A. List
B. R. Betzler

**August 2021**

M2TC-21OR0403032

OAK RIDGE National Laboratory

**ORNL/TM-2021/2121**

Transformational Challenge Reactor Program

# MECHANICAL PROPERTIES OF ADDITIVELY MANUFACTURED 316L STAINLESS STEEL BEFORE AND AFTER NEUTRON IRRADIATION: FY21

T. S. Byun
D. A. Collins
A. G. Le Coq
T. G. Lach
K. D. Linton
M. N. Gussev
J. W. Werden
M. R. McAlister
X. Chen
C. B. Joslin
J. K. Carver
F. A. List
B. R. Betzler

August 2021

M2TC-21OR0403032

Prepared by
OAK RIDGE NATIONAL LABORATORY
Oak Ridge, TN 37831-6283
managed by
UT-BATTELLE, LLC
for the
US DEPARTMENT OF ENERGY
under contract DE-AC05-00OR22725

**CONTENTS**

## LIST OF FIGURES

## LIST OF TABLES

## ACKNOWLEDGEMENT

This research was sponsored by the US Department of Energy Office of Nuclear Energy's Transformational Challenge Reactor program under contract DE-AC05-00OR22725 with UT-Battelle LLC. The authors thank Caleb Massey and Stephen Taller for their thoughtful review of this report before publication.

# Mechanical Properties of Additively Manufactured 316L Stainless Steel Before and After Neutron Irradiation: FY21


## ABSTRACT

This report presents the materials property data of additively manufactured (AM) 316L stainless steel (SS) accumulated for the assessment of core materials in the Transformational Challenge Reactor (TCR) program. The TCR manufacturing approach includes using the laser powder bed fusion (LPBF) method for metallic (316L and Inconel 718) components. To assess the mechanical performance of printed components in reactor-relevant conditions and build a property database for the AM materials, mechanical tests and evaluations were performed before and after neutron irradiation. Miniature tensile specimens were irradiated in the High Flux Isotope Reactor to 0.2, 2, 8, and 10 dpa at target temperatures of 300 and 600°C. Postirradiation evaluation for the 0.2 and 2 dpa specimens was performed during FY20 and FY21, and the results are presented and discussed in this document.

To obtain the baseline mechanical property data, uniaxial tension testing over a wide temperature range from room temperature (RT) to 600°C was performed for the same materials that were irradiated, including AM 316L SS in the as-built, stress-relieved, and solution-annealed conditions, as well as reference wrought (WT) 316L SS. Regardless of the postbuild heat treatment, the AM 316L SS showed higher strength than the WT 316L SS, but they had similar ductility. A statistical treatment of RT tensile data indicated that variations in the strength and ductility datasets of AM 316L steels were smaller than or similar to those of WT 316L SS. Additionally, 2D mapping of tensile properties for the stress-relieved AM plates also showed clear location dependence of the properties but with limited magnitudes.

Postirradiation tensile testing was conducted at RT, 300, 500, and 600°C for selected irradiation conditions. Additional tests were performed near the measured irradiation temperatures of 260 and 390°C for checking the impact of the difference between the targeted and actual irradiation temperatures. Neutron irradiation induced significant changes in the mechanical behavior of the AM SSs, including hardening and softening. Although the as-built 316L SS tested at 300°C after irradiation to 2 dpa at 390°C showed unstable plastic deformation (i.e., necking) immediately after yielding, the overall property changes of the as-printed alloy became much less significant after higher temperature (610 and 690°C) irradiations or when tested at different temperatures. Irradiation-induced ductilization was also observed in the higher strength materials (i.e., in as-built and stress-relieved conditions) after higher temperature (>600°C) irradiations. The strength change after irradiation was generally smaller in the relatively stronger materials (i.e., the as-built and stress-relieved AM SSs) than in the solution-annealed AM and WT SSs. Overall, these relatively lower strength 316L SSs retained higher ductility in the irradiation conditions tested, but the stronger 316L SSs demonstrated a similar level of ductility after higher temperature irradiations. For the AM 316L materials, no embrittlement was observed within the test and irradiation conditions of the experiment.


## 1. INTRODUCTION

Reactor core materials in advanced nuclear energy systems will be subject to high-temperature and high-dose neutron irradiations, which will significantly change the microstructures and local chemistries of the materials and thus degrade their mechanical, chemical, and physical properties [1]. Therefore, the core materials for any high-performance reactor will require excellent high-temperature mechanical properties, high-radiation resistance, and high-corrosion resistance, in addition to the feasibility of manufacturing processes. The 300 series austenitic stainless steels (SSs) are widely used in the reactor core and coolant

system components of current nuclear power plants and have been among the key candidate structural materials for advanced future reactors, including sodium-cooled fast reactors and fusion energy systems [2-6]. The austenitic alloys have been consistently used for nuclear applications because they provide a good combination of strength, ductility, toughness, and oxidation-corrosion resistance over an exceptionally wide temperature range [7]. Their austenitic (i.e., face-centered cubic) structure is highly stable within and beyond the possible reactor operation temperature ranges, which should be the root cause for retaining such good properties in reactor environments [2,4,5,7]. In particular, their high phase stability, high ductility, and toughness lead to excellent resistance to radiation damage and embrittlement during in-reactor service [2,7].

Recent research efforts confirmed that austenitic SSs are highly suitable for additive manufacturing of complex shaped reactor components [8-11]. This is likely because the fast cooling that occurs during the AM process prevents the formation of the high-temperature ferrite (i.e., δ-ferrite) phase during cooling, which is metastable and undergoes degradation at high temperatures caused by phase decomposition and segregation. The high oxidation resistance [7] might help form relatively clean boundaries between printed layers. Multiple AM technologies have advanced rapidly in recent years and are now poised to revolutionize the design and manufacture of complex components in a fully computerized manner [9]. Examples of such key AM technologies that are deemed relevant to nuclear reactor core structures include the laser powder bed fusion (LPBF) process via selective laser melting or electron beam melting, laser-directed energy deposition, and binder jetting combined with a chemical vapor infiltration (CVI) process for ceramics [8].

The AM technologies will provide many opportunities and challenges if they are used to build a nuclear reactor core. These technologies offer enormous flexibility in designing and building complex components that can be cost prohibitive with traditional manufacturing methods. Furthermore, AM material properties can be tailored by changing processing parameters, such as scan speed, laser power, powder feedstock purity, and powder layer thickness [12-14]. In particular, the size and orientation of the fine-grained dislocation cell structure in metallic materials can be easily controlled by changing processing parameters [10,15-17] or applying postbuild heat treatments [13]. However, because the LPBF process usually produces a very fine but metastable microstructure due to fast cooling in solidification, there are still many unknowns and adverse effects regarding the microstructural and chemical stability of AM materials in high-temperature, corrosion, and irradiation environments. The as-printed materials were observed to have increased room temperature (RT) yield strength (YS) but less work hardening because of a characteristic microstructure of fine grains and dislocation cells formed during the localized rapid solidification [15,18-20]. Recent test results indicate that these fine-grained structures with mobile dislocations can shorten the high-temperature creep life [8,10,21]. Furthermore, the fracture toughness of AM 316L SS could be negatively affected by the increased porosity from the build process, structural anisotropy relative to the build direction, and inclusions from impurities in the feedstock powder [12,22]. Neutron or ion irradiation could also significantly affect the behaviors (i.e., shortened creep life and reduced fracture toughness) observed in AM alloys [11,23-25].

The Transformational Challenge Reactor (TCR) program has fully adopted the LPBF process and binder jetting CVI methods and is using them to build most of its reactor components [8,9,26]. The extensive knowledge of conventionally manufactured 316L SS combined with the well-established AM processing route makes the 316L alloy an ideal core structural material for TCR. Therefore, the main metallic components that constitute the TCR core structures will be the 316L SS parts printed via the LPBF process [8,10].

To ensure successful reactor core design using the AM components, assessing the materials performance and structural integrity of the AM components is very important. These components must provide multiple essential functions to transfer heat to the He gas coolant and mechanically support the main core

components, such as nuclear fuel elements and moderator assemblies. The TCR core structural materials are exposed to the He gas coolant with an outlet temperature of ~500°C and to the high-flux neutron irradiation on the order of tens of displacements per atom. Because the materials degradation caused by the coolant corrosion, void swelling, and He embrittlement [2-6] will be insignificant in the TCR environment, some of the high-temperature mechanical properties—including deformation and fracture, creep, and creep-fatigue properties—must be evaluated for the assessment of the core materials [21].

Therefore, this research aimed to evaluate the tensile deformation and failure properties of the AM 316L SSs before and after irradiation to inform the assessment of their in-reactor performance. The AM 316L was tested in three different conditions: as-built, stress-relieved, and solution-annealed. The reference wrought (WT) 316L alloy in the solution-annealed condition underwent the same tests for comparison. Baseline testing included uniaxial tensile testing at various temperatures and in situ deformation and failure testing in scanning electron microscopy (SEM). Postirradiation examination (PIE) for the 316L alloy in all four material conditions included static tensile testing at RT, 265, 300, 390, 500, and 600°C.

This milestone document reports the key mechanical property data for the AM 316L SSs accumulated in the program. The discussion in this report focuses on the baseline tensile characteristics, the effect of postbuild heat treatments, and the effect of radiation on tensile deformation behavior for the 316L SSs in the four different conditions. Furthermore, the statistical and spatial distribution behaviors of mechanical properties and unique microstructural characteristics are discussed in detail. The main addition from this fiscal year's execution is the PIE data, which show various radiation effects on mechanical properties, such as irradiation hardening and softening, ductility reduction, and irradiation-induced ductilization. The conclusion provides guidance on the optimized condition of the AM 316L alloy (i.e., stress-relieved condition) and an assessment of the AM 316L SS as the key structural material for TCR core application.

## 2. EXPERIMENTAL DETAILS

### 2.1. Materials and Specimens for Baseline and Postirradiation Evaluation

The materials tested in this research include AM 316L SS and its reference alloy or WT 316L SS; the chemical compositions for these materials are presented in Table 1. All AM 316L SS specimens (SS-J2 and SS-J3 type flat tensile specimens) were machined from the two ~12 mm thick plates printed by the LPBF process in Concept Laser M2, a GE AM system. The build identification number was 20190208, which is the printing date. Such date-based materials identifiers were used in specimen group IDs in the build, mechanical property data, and characterization records. Individual tensile specimens had their own IDs that could be traced back to their position information in the build because the two plates used were numbered 1 and 2. These two plates were printed in parallel by using two laser-nozzle components in the Concept Laser M2 system along with other plates and rods. The base material used for printing was 15–45 μm powder feedstock from Praxair, the nominal composition of which is presented in Table 1. The following typical or vendor-recommended processing parameters were used for the build: 370 W laser power, 1,350 mm/s scan speed, 130 μm beam size, 90 μm hatch spacing, and 50 μm layer thickness. These parameters were held constant throughout the printing process in an Ar gas environment.

**Table 1. Chemical compositions of 316L SSs: AM 316L (Praxair powder) and WT 316L alloy (in wt %).**

| Materials | Fe | Cr | Ni | Mo | Mn | Si | N | Cu | Co | C | P | O |
|---|---|---|---|---|---|---|---|---|---|---|---|---|
| AM 316L (Praxair powder) | Bal. | 17.1 | 12.1 | 2.41 | 1.19 | 0.46 | 0.01 | 0.01 | 0.1 | 0.006 | <0.005 | 0.05 |
| WT 316L | Bal. | 16.7 | 10.2 | 2.03 | 0.63 | 0.53 | 0.047 | - | - | - | 0.027 | - |

The SS-J2 type miniature tensile specimens were taken from the two thick plates in the as-printed condition through electrical discharge machining. The SS-J2 specimens have a nominal gage section of 5 × 1.2 × 0.5 mm (Figure 1), all of which were in the build (*Z*) direction corresponding to the growth (i.e., layer stacking) direction in the LPBF process. The width and thickness directions of flat tensile specimens coincided with the same directions of the plates (i.e., *X*- and *Y*-direction, respectively). The tensile testing of the specimens with the perpendicular (*X*-) direction was not included in this research, mainly for simplicity, because the result of an earlier work [8] indicated that the effect of specimen orientation was insignificant and inconsistent at different test temperatures.

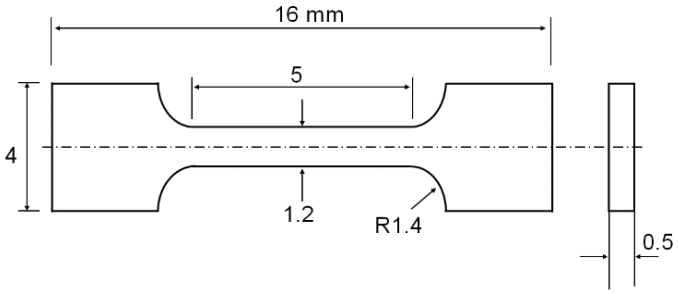


**Figure 1. SS-J2 miniature tensile specimen for shoulder loading (not to exact scale).**

Part of the AM 316L tensile specimens was heat treated for stress relieving at 650°C for 1 hour or for solution annealing at 1,050°C for 1 hour. As a result, the AM 316L SS specimens were tested in the as-built, stress-relieved, and solution-annealed conditions, and the WT 316L SS underwent the same testing as a reference alloy for comparison. The reference WT 316L SS was tested in a solution-annealed condition (~1,040°C for at least 1 hour), which was provided by Sandmeyer Steel Company in Philadelphia, Pennsylvania. All WT 316L tensile specimens were tested in the perpendicular (lower-ductility) direction to the rolling direction to coincide with the AM 316L specimens tested in the lower-ductility (Z) direction.

The contents of all main alloying elements, from Cr to Mn in Table 1, are lower in the WT 316L, but the two alloys have close Cr equivalents (20.2 and 19.6% for AM and WT 316L alloys, respectively); therefore, they should have similar phase (i.e., austenite) stability [27]. Assuming that both have sufficiently low C contents (as seen in Table 1) and thus limited carbide dispersion hardening, their mechanical behaviors might mainly depend on microstructural features from the processing route, such as grain size, dislocation density, and pore density.

## 2.2. Specimens for Measuring Spatial Distribution of Properties

Many sets of tensile property data were obtained under the scope of the Digital Platform thrust in the TCR program. Among those, two selected datasets are introduced in this report to elucidate the location dependence of tensile properties in the 3D printed 316L alloy. This section describes the geometry of TCR 20201119 Phase 0 Build 1, its heat treatment, and the tensile testing conditions. Figure 2 is a top view of the 20201119 build showing the positions of the two cube parts, 11 and 21, in which tensile property distributions are discussed in this report. These parts were nominally 40 × 40 × 40 mm cubes. In Figure 2, the green regions represent the parts in the 20201119 for which nonirradiated tensile data were collected, and the small gray regions are the nominal locations from which the tensile specimens were machined. The locations of the cubes in the build likely affected their mechanical properties because the differences in proximity to other parts and to the inert gas inlet of the 3D printer would have influenced their convective cooling and thus their mechanical properties. Furthermore, the difference in cooling rates

at the surface and in interior locations are also expected to influence the resulting mechanical property distribution.

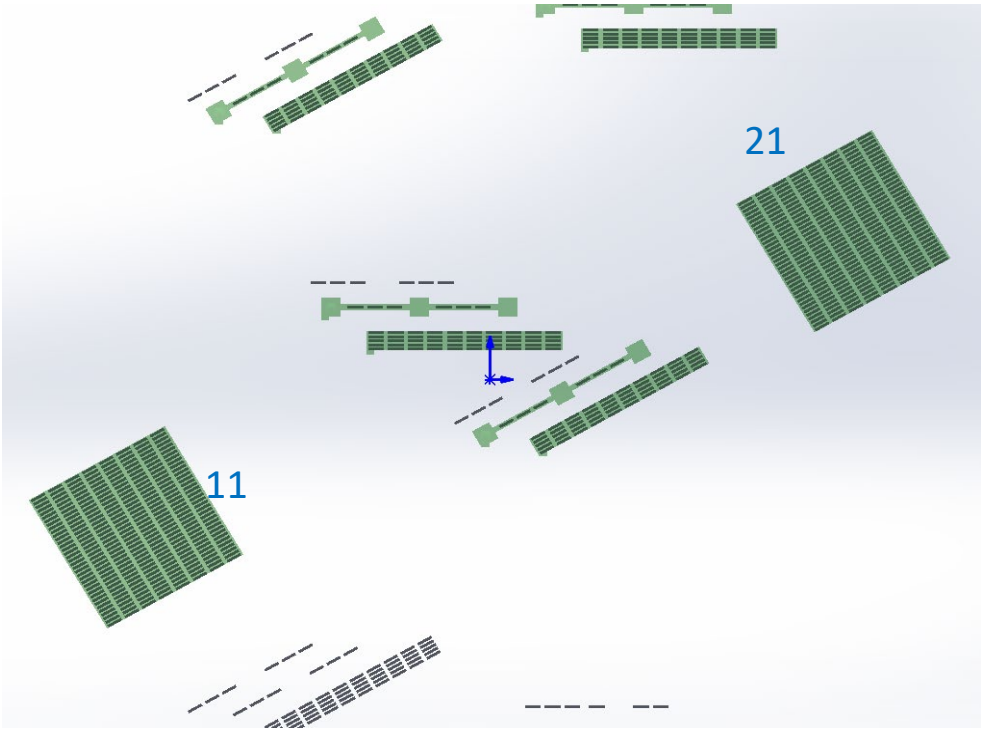


**Figure 2. Positions of the cube parts in the 20201119 build (part 21 is located (+180, +80) mm relative to the part 11.)**

After printing, the build was heat treated to relieve residual internal stresses. The nominal procedure was to heat the build to 650°C at a rate of 10°C/min in the air, hold at 650 ± 10°C for at least 30 min, cool to 480°C at a rate of 7°C/min, and then air-cool to RT. The actual schedule was to heat to 670°C at a rate of 7.5°C/min. The build was allowed to cool to 640°C and held for 64 min. The build was cooled to 480°C at a rate of 2.7°C/min before air-cooling. It is unclear what thermal gradients were present in the treatment furnace during the procedure. This heat treatment applies to all 20201119 build parts. The parts in the stress-relieved condition were machined into SS-J3 tensile specimens, which have the same profile dimensions as those shown in Figure 1 but are thicker (0.75 mm, or ~30 mil). The SS-J3 nonirradiated samples were tested in an ambient condition at an elevated displacement rate of 0.5 mm/min (a nominal strain rate of ~10% per minute) until fracture.

### 2.3. Irradiation Conditions of Tested Specimens

To evaluate the effects of radiation on the tensile properties of the 316L SSs under the four conditions, the SS-J2 tensile specimens were irradiated at ORNL's High Flux Isotope Reactor (HFIR) using rabbit capsules [28,29]. Each capsule contained 36 SS-J2 specimens, 12 of which were in the as-built condition and eight of which were specimens for each of the other three conditions. Multiple SiC passive temperature monitors (TMs) were also stacked together in the capsules. Neutron irradiation of first four rabbit capsules—GTCR01, GTCR02, GTCR04, and GTCR05—was completed at HFIR to obtain the target displacement damages of 0.2 and 2 dpa at 300 and 600°C at a displacement damage rate of ~1 μdpa/s. Irradiation was continued for the remaining capsules, GTCR03 and GTCR06, to achieve higher doses. Irradiation doses and temperatures for the four capsules are summarized in Table 2 in which the measured temperature data are from SiC TMs [28,29], and the readings from three SiC TMs were

averaged for each measured TM temperature listed in the table. The sample temperatures were also evaluated based on the measured TM temperatures. The differences between the target and measured irradiation temperatures are significant for the first three capsules, although each measured temperature can still represent a low-temperature or a high-temperature irradiation. For the sake of simplicity, the TM temperatures are used in the following figures and descriptions.

**Table 2. Irradiation conditions for the four capsules irradiated to 0.2 and 2 dpa.**

| Capsule ID/HFIR location | Dose (dpa) | Design temp. (°C) | TM temp. (sample temp. ± 1σ) (°C) |
|---|---|---|---|
| GTCR01/B3(HT)-6 | 0.2 | 300 | ~260 (250 ± 4) |
| GTCR02/A4(PTP)-6 | 2 | 300 | ~390 (376 ± 25) |
| GTCR04/B3(HT)-4 | 0.2 | 580 | ~690 (673 ± 45) |
| GTCR05/B4(TRRH)-3 | 2 | 600 | ~610 (600 ± 11) |

Although a large set of 144 SS-J2 specimens was irradiated in the four dose-temperature conditions, only 52 selected specimens among those irradiated to 0.2 and 2 dpa have been tested so far. Testing for the remaining and highest dose specimens will continue in the future. Radiation effects discussed in later sections are based on the tensile test results of the AM and WT materials irradiated to 0.2 and 2 dpa.

## 2.4. Baseline and Postirradiation Tensile Testing

Uniaxial tensile testing for SS-J2 specimens was performed by using two mechanical testing systems equipped with vacuum furnaces for temperature control: the MTS-858 servohydraulic testing system at the Low Activation Materials Design and Analysis (LAMDA) laboratory for preirradiation testing and the static Instron-5kN system at the Irradiated Materials Examination and Testing (IMET) facility for postirradiation testing. All tension tests were performed at a nominal strain rate of $5 \times 10^{-4}$ $s^{-1}$ (displacement rate = 0.15 mm/min) by using shoulder loading grip sets [30]. Raw data or load-displacement data up to failure were recorded and used to determine the common engineering strength and ductility parameters, including YS, ultimate tensile strength (UTS), uniform elongation (UE), and total elongation (TE). If not specified otherwise, tensile testing and data analysis were performed by following the standard testing procedure in ASTM E8/8M and E21 [31,32]. Table 3 lists the test temperatures for irradiated and nonirradiated SS-J2 tensile specimens in the four different conditions. The high cost and time for handling highly radioactive specimens limited the number of tests for the irradiated materials. Except for the multiple RT tests per condition before irradiation, which is for a statistical treatment of datasets, one test was performed per irradiation and test condition.

**Table 3. Tensile test matrix for irradiated and nonirradiated SS-J2 316L specimens.**

| Materials | Test temp. before irradiation (°C) | Test temp. after irradiation (°C) | | | |
|---|---|---|---|---|---|
| | | 0.2 dpa, 260°C | 0.2 dpa, 690°C | 2 dpa, 390°C | 2 dpa, 610°C |
| AM 316L (as-built) | RT(20), 200, 300, 400, 500, 600 | RT, 260, 300 | RT, 600 | RT, 300, 390, 500 | RT, 300, 500, 600 |
| AM 316L (stress-relieved) | RT(7), 200, 300, 400, 500, 600 | RT, 260, 300 | RT, 600 | RT, 300, 390, 500 | RT, 300, 500, 600 |
| AM 316L (solution-annealed) | RT(9), 200, 300, 400, 500, 600 | RT, 260, 300 | RT, 600 | RT, 300, 390, 500 | RT, 300, 500, 600 |
| WT 316L (reference) | RT(8), 200, 300, 400, 500, 600 | RT, 260, 300 | RT, 600 | RT, 300, 390, 500 | RT, 300, 500, 600 |

*RT(#) is the number of tensile tests at RT; for all other cases, one valid data was obtained at each test temperature.*

### 2.5. Microscopy for Initial Microstructures

The initial microstructures of the AM 316L and WT 316L SSs were examined by using a TESCAN MIRA3 SEM equipped with an Oxford Instruments electron backscatter diffraction (EBSD) detector and an FEI Talos 200 keV scanning transmission electron microscope (STEM) equipped with a X-field emission gun high-brightness field emission source, bright field (BF) and multiple annular dark field detectors, and a quadrupole FEI ChemiSTEM energy dispersion x-ray spectroscopy collection system. The EBSD images (i.e., the colored inverse pole figure [IPF] maps) for grain structures and high-resolution BF images that show subgrain and dislocation structures were obtained from the SEM and STEM equipment, respectively. The SEM-EBSD images were obtained directly from the polished tensile specimen surfaces, and the cross section samples for STEM were taken from the tensile specimens by using an FEI Quanta focused ion beam (FIB)/SEM. The lamellae were lifted out by using 30kV Ga ions, thinned to electron transparency using 8 and 5 kV Ga ions, and fine polished at 2 kV. The lamellae were then transferred to a Fischione Model 1040 Nanomill in which damage from the FIB was removed by using 900 eV Ar ions.

## 3. PREIRRADIATION PROPERTIES

### 3.1. Initial Microstructures of AM and WT 316L Stainless Steels

Because the rapid melting-cooling and remelting-cooling cycles occur during LPBF printing, the as-printed 316L SS shows many unique microstructural features that are distinctly different from those observed in common annealed or cold-worked SSs [12]. The austenite grains in AM 316L alloy are much smaller when compared with the fully annealed austenite grain aggregates, and they have elongated shapes in most cases. Furthermore, each rapid heating-cooling cycle occurs in a small local volume of the material, which induces an intense thermal stress fields and activates dislocation slip systems for relaxation. This results in a high-density dislocation network, often with a well-developed cellular structure [15,18-20]. Therefore, the behavior of the as-built 316L SS shows a unique mechanical behavior that differs from that of annealed austenitic SSs.

Figure 3 compares the grain structures of the AM 316L SSs under different conditions, including the as-built, stress-relieved (650°C/1 h), and solution-annealed (1,050°C/1 h) conditions. These are also compared with the grain structure of WT 316L SS. The AM 316L SS in the as-built condition has a very fine microstructure with mostly irregularly bent or crescent-shaped fine grains. This characteristic structure is most likely the remnants of the melting pools, many of which were partially remelted multiple times by subsequent laser beam passes [9]. There are often relatively smaller grains or grain groups between the clusters of larger crescent-shaped grains. Neither the postbuild annealing treatment at 650°C nor the postbuild annealing treatment at 1,050°C caused the apparent grain growth; the average intercept lengths of grain boundaries were measured at 13–15 μm for all three AM 316L conditions [10]. Figure 3 confirms that the grain structures of the AM steels are different from those of the WT 316L steel, which has much larger (~47 μm on average) and equiaxial grains with many straight grain or twin boundaries. Additionally, the EBSD IPF maps in Figure 3 indicate that texturing exists but is generally very weak. In the authors' previous work for the same material [8], slightly elevated fractions of some specific grain families (e.g., [101]-oriented grains in the [100]-map) were observed, but the degree of texturing in the AM 316L steel was at the level routinely observed in annealed SS plates, indicating a negligible consequence regarding mechanical behavior and material performance [8].

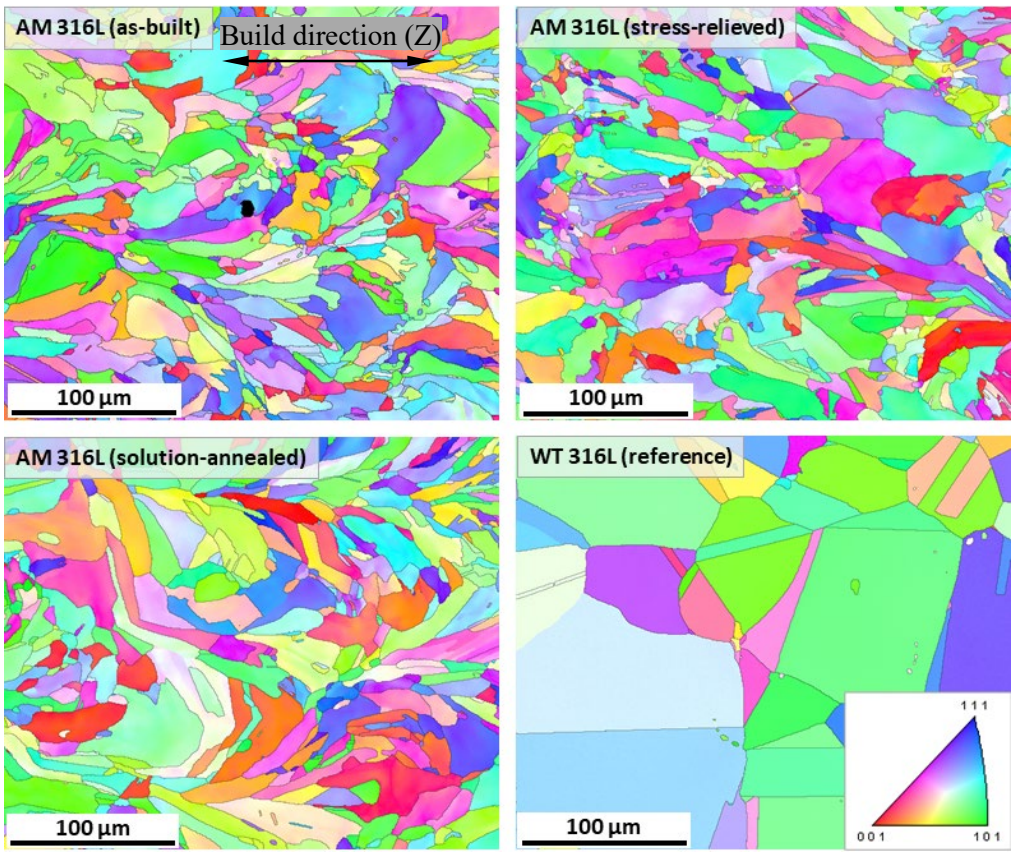


**Figure 3. Microstructures (EBSD IPF maps) of AM 316L in the as-built, stress-relieved, and solution-annealed conditions. The build direction (*Z*) is horizontal, and the IPF maps are colored relative to the building (i.e., horizontal) direction.**

The STEM images for AM 316L SS samples in all four conditions were taken in the BF condition, as shown in Figure 4. Although the EBSD-IPF images in Figure 3 indicate that the grain level structure of the as-built AM 316L does not significantly change after the two postbuild heat treatments, its subgrain structure is expected to change as a result of the annealing treatments because the gradual change of baseline tensile properties is observed, as described in the Section 3.2. The STEM micrographs in Figure 4 show how the microstructure of AM 316L SS changes with annealing temperature. The images were based on two beam conditions from the [001]-type zone axis for the as-built specimen and [011]-type zone axis for the other three conditions. Unfortunately, tilt limits prevented imaging on the same zone axes for all specimens; however, if present, similar dislocation structures, such as cellular structures, could be found on each zone axis. The as-built and stress-relieved (650°C anneal) conditions both have a dislocation cellular structure [17,33-35], as indicated by the blue arrows. The cellular structure was completely removed by annealing at 1,050°C. As shown in the following sections, removing the cellular structure after annealing not only reduces the YS of the steel but also likely increases the work hardenability as the dislocation structure becomes no longer built into the microstructure.

Oxide nanoscale inclusions are also found in the microstructure of the AM SS, as indicated by the red arrows in Figure 4. These oxides are likely from the native oxide in the feedstock powder [8,9,12]. As explained in Morrow et al. [12], in the as-built and stress-relieved conditions, the oxide particles are Si- and Mn-rich, whereas in the solution-annealing treatment, the oxide particles change from Si-Mn-Al-Cr-rich oxides to Cr-Mn-rich oxides with minimal or no Si. These oxide particles might be relatively stable during deformation and irradiation and are expected to persistently affect the failure process of AM SSs,

regardless of material conditions. Additionally, the microstructure of the reference WT 316L SS resembles that of the AM 316L in the solution-annealed condition but without the oxide inclusions. It was also shown that the WT alloy, like the solution-annealed AM material, still had dislocations, but there was no compositional variation within the matrix, unlike the as-built and stress-relieved AM materials. The cellular structure in the as-built and stress-relieved AM materials has Cr segregation to the cell walls, which is also commonly found in AM SSs [14,36].

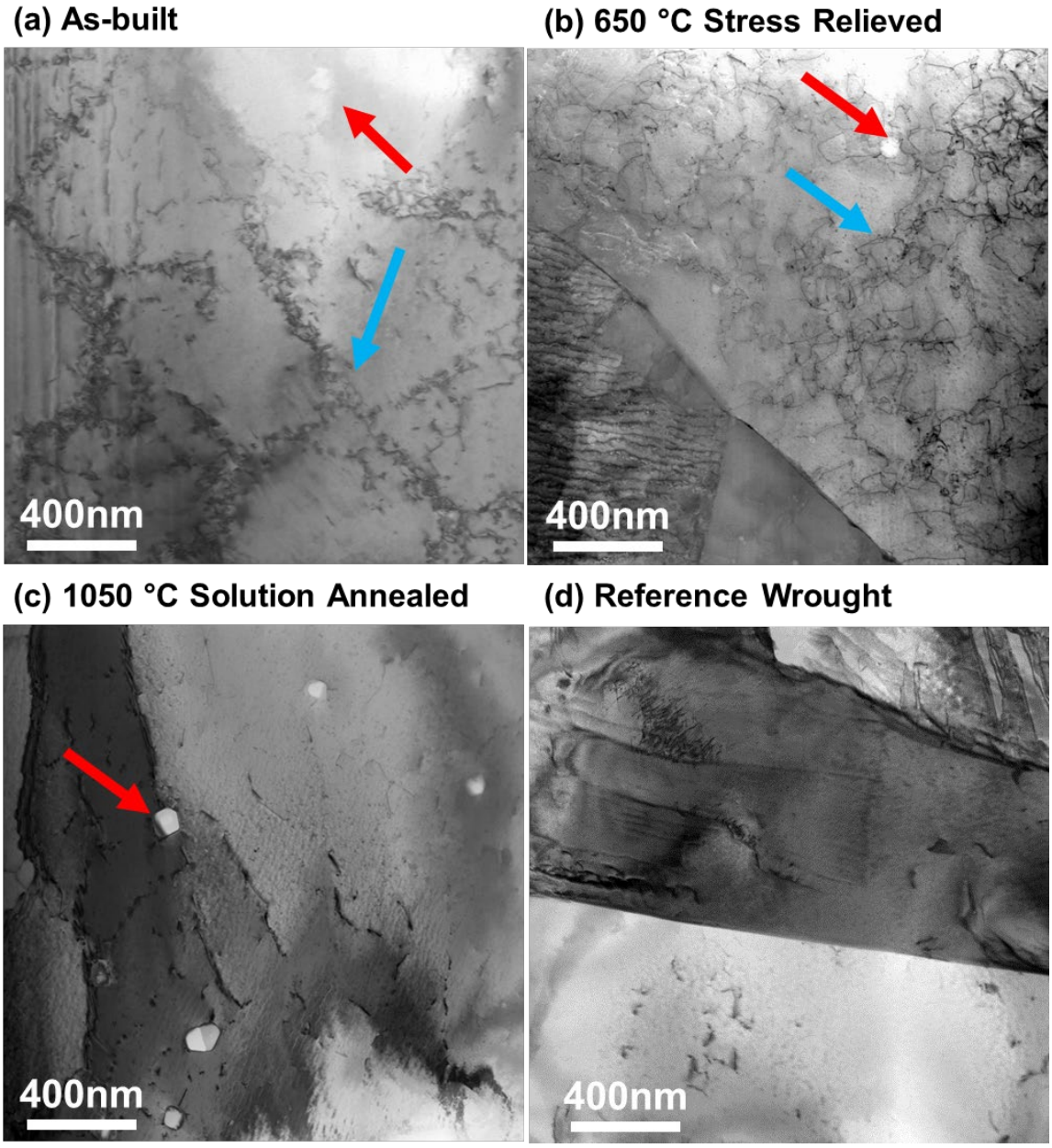


**Figure 4. STEM BF micrographs of AM 316L SS in the (a) as-built, (b) stress-relieved, and (c) solution-annealed conditions. (d) The reference WT 316L SS. The blue arrows in (a) and (b) point to regions where dislocation cellular structures are present. The red arrows in (a), (b), and (c) point to oxide inclusions in the AM steel. The reference material in (d) has neither cells nor oxide inclusions.**

### 3.2. Temperature Dependence of Strength and Ductility

As a result of the rapid melting-cooling cycles in the LPBF process, the as-printed 316L SS usually shows many unique microstructural features, including fine curved-grain structures and high-density dislocation cell structures [15,18-20]. Postbuild annealing treatments can modify the as-built microstructure and result in mechanical behavior changes, progressing toward that of the fully annealed WT 316L. Along with the temperature dependence of tensile property parameters, the effects of postbuild annealing treatments on those parameters are discussed in this section [10,11]. Figures 5 and 6 compare the baseline strength and ductility data determined from the load-displacement data. The RT data presented in these plots are the average values from multiple specimens and are given with their standard deviation error bars; the results of statistical analyses of these RT data are discussed in Section 3.3.

Figure 5(a) compares the YS data obtained after the four different processing routes. YS decreases monotonically with the test temperature over the range of RT to 600°C, and all four 316L conditions show similar temperature dependencies. The WT 316L SS—which is in a hot-rolled, fully annealed condition—shows the lowest YS among the four conditions, whereas the as-printed 316L (AM 316L) demonstrates the highest strength at all test temperatures. A gradual change of YS is observed between two extreme cases: (1) applying a stress-relieving treatment at 650°C for 1 h, which reduced the strength of AM 316LSS at all test temperatures, and (2) annealing the solution at 1,050°C for 1 h, which further decreased the YS to about two-thirds the level of the YS in the as-built condition.

The AM 316L alloy can still retain high YS, even after the 1,050°C solution annealing; its YS is higher than that of the WT 316L alloy over the entire test temperature range. This might be because the solution treatment has removed much of the built-up dislocations and residual stresses; however, as shown in Figure 4, it did not induce a significant grain growth. The strengthening effect from the characteristically fine microstructure of AM materials still contributes to the strengthening of the material, even after high-temperature (1,050°C) annealing.

Figure 5(b) compares the UTS data of the four AM and WT 316L SSs. Overall, high UTS values (>550 MPa) are measured for all 316L variants at RT, and they decrease with test temperature, except for the WT 316L SS. The differences in UTS values among the four different processing routes are much smaller than those in the YS data. This is because the UTS is determined at the maximum load in each load-displacement record and is an engineering parameter measured at a relatively large strain or in a later part of tensile deformation in which the stress-strain curves of AM 316L and WT 316L SSs become closer. Also, the dependence of strength in three AM 316L materials is monotonic, whereas that for the WT 316L alloy shows a local minimum in strength at around 200°C.

Figure 6 shows the ductility data for the AM 316L and WT 316L SSs. In these datasets, the UE and TE rapidly decrease with the test temperature in the range of RT to 200°C, and their temperature dependence becomes much less obvious in the higher temperature range (200–600°C). Over this elevated-to-high temperature range, the temperature dependencies of ductility parameters are more similar to those of UTS rather than to those of YS, although they are relatively small and more varied.

The stronger 316L materials generally show lower ductility, as observed in most of the metallic materials, meaning that relatively lower ductilities are measured from the stronger AM 316L materials. For example, the lowest uniform ductility measured is ~15%, which was measured at 300°C from the as-built 316L. Only small differences between UE and TE (4–10%) are measured because of their limited necking deformation. Also, a local ductility minimum exists in the temperature range of 300 to 500°C before the parameters increase with temperature. This reduced ductility is likely due to the dynamic strain aging (DSA) effect [37,38], which is discussed further in Section 3.4.

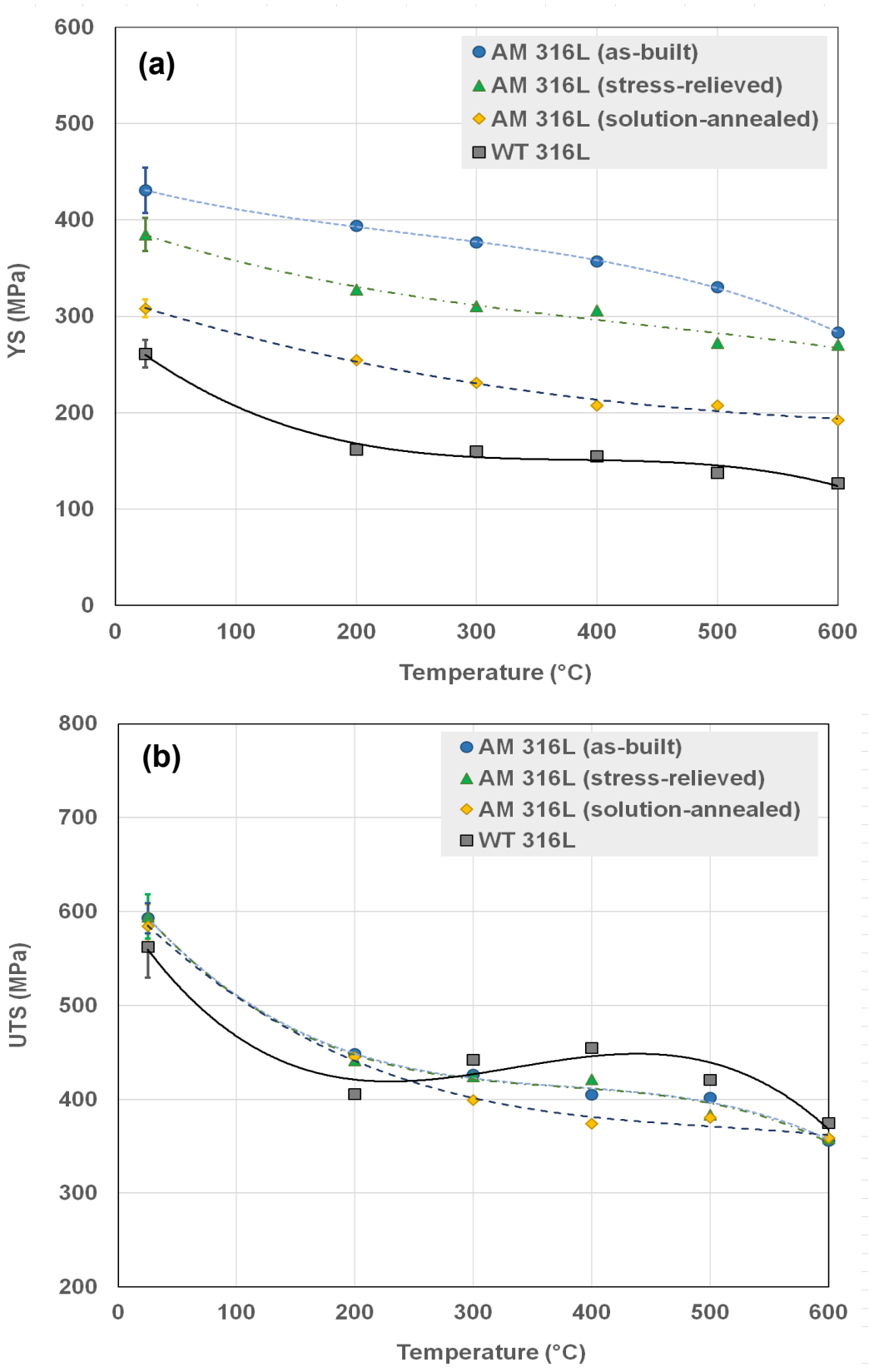


**Figure 5. Temperature dependence of tensile strength: (a) YS and (b) UTS in 316L SSs after four different processing routes.**

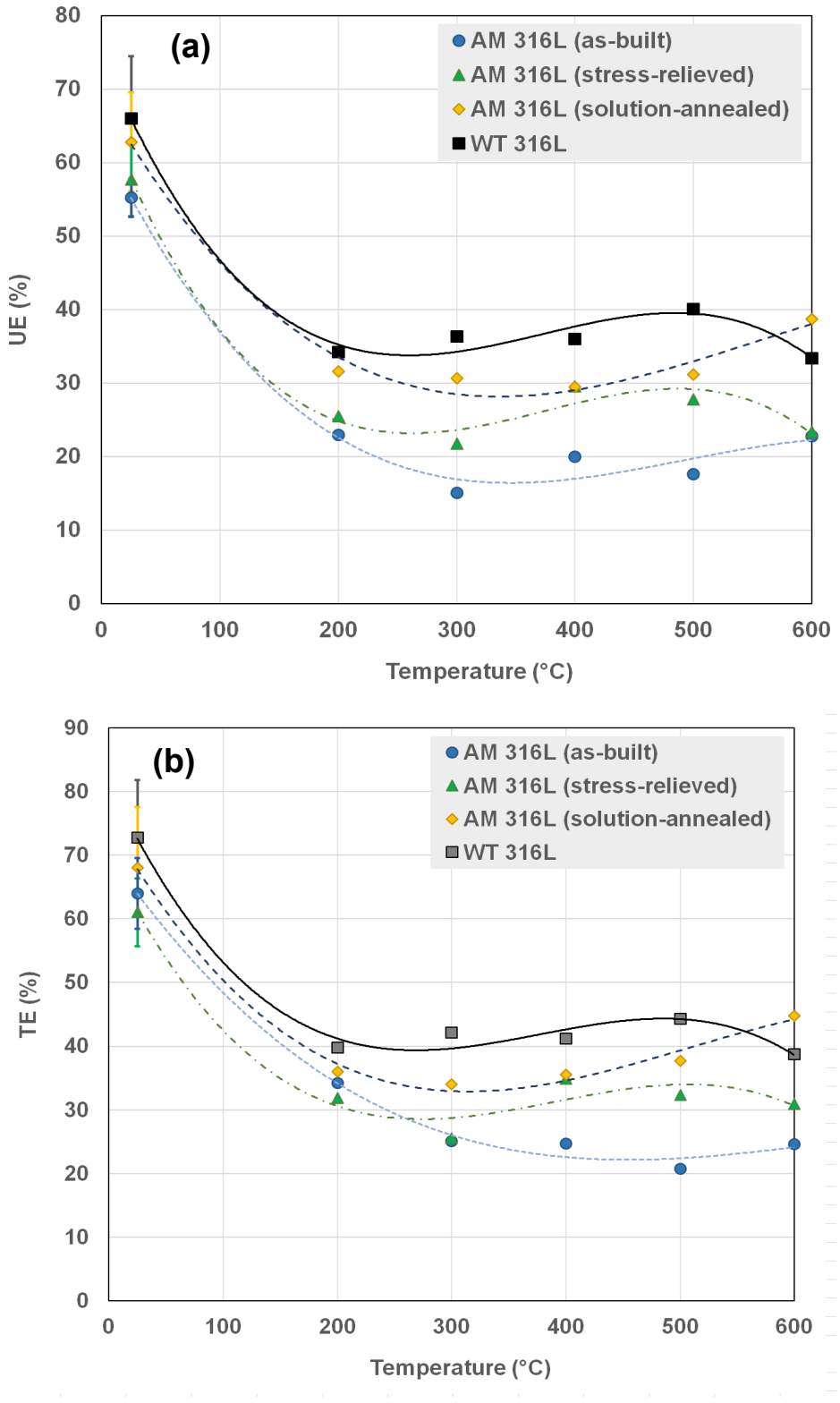


**Figure 6. Temperature dependence of tensile ductility: (a) UE and (b) TE in 316L SSs after four different processing routes.**

### 3.3. Statistics of Room Temperature Tensile Property Data

Although the LPBF manufacturing parameters are precisely controlled by a computerized system, many factors could affect the uniformity of local material quality. For example, the input laser powder could fluctuate and alter the local melting-cooling cycles and the position of the melting pool, particularly the distance from the surface, and it could also significantly affect the cooling rate, its uniformity and resultant porosity. Many of these varying factors in the AM process are expected to contribute to the variation of mechanical properties. Therefore, to elucidate the statistical behavior of the AM materials, multiple tensile tests were performed at RT to measure variations in the tensile properties. Sample sizes ($N$) were between seven and 20 for the 316L materials in the four different conditions.

The results of statistical treatment for the key tensile parameters are summarized in Table 4. For the strength datasets, relatively larger standard deviations were calculated for the WT 316L SS and the AM 316L SS in the stress-relieved condition, whereas the AM 316L steel in the solution-annealed condition demonstrated the lowest deviation in both of its strength datasets. The AM 316L in the as-built condition has relatively low standard deviations among the test materials, whereas the WT 316L has the highest variations in its strength datasets. Similar behavior was observed in the ductility datasets; the relatively lower standard deviations—2.6% for UE and 5.6% for TE—were measured for the AM 316L in the as-built condition. Higher ductility variations are clearly calculated for the 316L SSs with relatively lower strengths, which are the AM 316L SS in the solution-annealed condition and the WT 316L SS; this is also in a very similar solution-annealed condition.

**Table 4. Summary of RT tensile property data from SS-J2 tensile specimens: mean values and standard deviations (in parentheses).**

| Materials | N | YS (MPa) | UTS (MPa) | UE (%) | TE (%) |
|---|---|---|---|---|---|
| AM 316L (as-built) | 20 | 430.8 (11.6) | 593.1 (16.0) | 55.2 (2.6) | 64.0 (5.6) |
| AM 316L (stress-relieved) | 7 | 385.1 (17.2) | 594.7 (23.4) | 57.7 (5.0) | 61.0 (5.4) |
| AM 316L (solution-annealed) | 9 | 308.2 (4.9) | 584.1 (9.4) | 62.8 (6.7) | 68.0 (9.6) |
| WT 316L (reference) | 8 | 261.1 (14.3) | 562.2 (32.5) | 66.0 (8.4) | 72.8 (9.0) |

This type of characteristic behavior in tensile properties is also confirmed by treating the datasets with the Weibull statistics [39] in which the probability ($P$) of failure or an event is given by:

$$P(i) = (i - 0.3)/(N + 0.4), \quad (1)$$

where $i$ is the rank of the data, and $N$ is the sample size [40]. In each Weibull plot, the slope of the linear line that represents data variability is called the *Weibull modulus (m)*. This is a dimensionless parameter of the Weibull distribution, which was originally used to describe variability in the measured failure strength of brittle materials [41]. It was attempted here to treat the two tensile property parameters of YS and TE with the statistics and to express them in Weibull plots because the variability of deformation and failure mechanisms within each material can be measured [41,42].

Figures 7(a) and 7(b) compare the Weibull plots for the strength and ductility parameters, respectively. The regression lines indicate that the Weibull moduli of AM 316L SSs are in the range of 22 to 66, whereas that of the WT 316L is about 22, which is the lowest level among the AM 316L datasets. The as-built and solution-annealed AM 316L steels show the two highest $m$ values, which actually indicate the two lowest variabilities. As shown in the standard variation of TE data, the fully annealed materials, WT 316L and AM 316L in the solution-annealed condition show the two lowest Weibull moduli among the

316L materials: 8.4 and 7.6, respectively. The as-built AM 316L alloy demonstrates the highest modulus ($m$ = 13.7) or lowest variability among the test materials.

Contrary to the expectation that the AM materials might show higher variations in their properties, the AM 316L SSs were confirmed to show evidence of opposite behavior. A high variation in a property dataset might be caused by a nonuniform microstructure, so the fine microstructure of AM 316L is assumed to not act as a highly heterogeneous material. That is, the TE data of AM 316L SS in the as-built condition can show the highest Weibull modulus, as shown in Figure 7(b), because the combination of very fine microstructure and high residual stress on such a small scale could lead to more uniform deformation. In general, a finer microstructure can absorb more mismatching strain at its higher density boundaries but build less local stress as the internal stress from any mismatch displacement is proportional to the crystal size. Therefore, the opposite might occur in the reference 316L SS because its much coarser microstructure could cause high local stress concentration at high mismatch grain boundaries during deformation; thus, it might result in higher property variability.

The Weibull modulus data indicate much higher variabilities in ductility data than in strength data. The moduli measured from the ductility data shown in Figure 7(b) are much smaller than those of the strength data shown in Figure 7(a). Table 4 also confirms that the ductility data show higher ratios of deviations to the ductility data. For example, the 5.6% TE deviation in the as-built AM 316 is about 9% of the TE (64%), whereas the 16 MPa UTS deviation is only 2.7% of the UTS (593.1 MPa). In Figures 7(a) and 7(b), a similar degree of ratios is found between the Weibull moduli of the strength and ductility parameters.

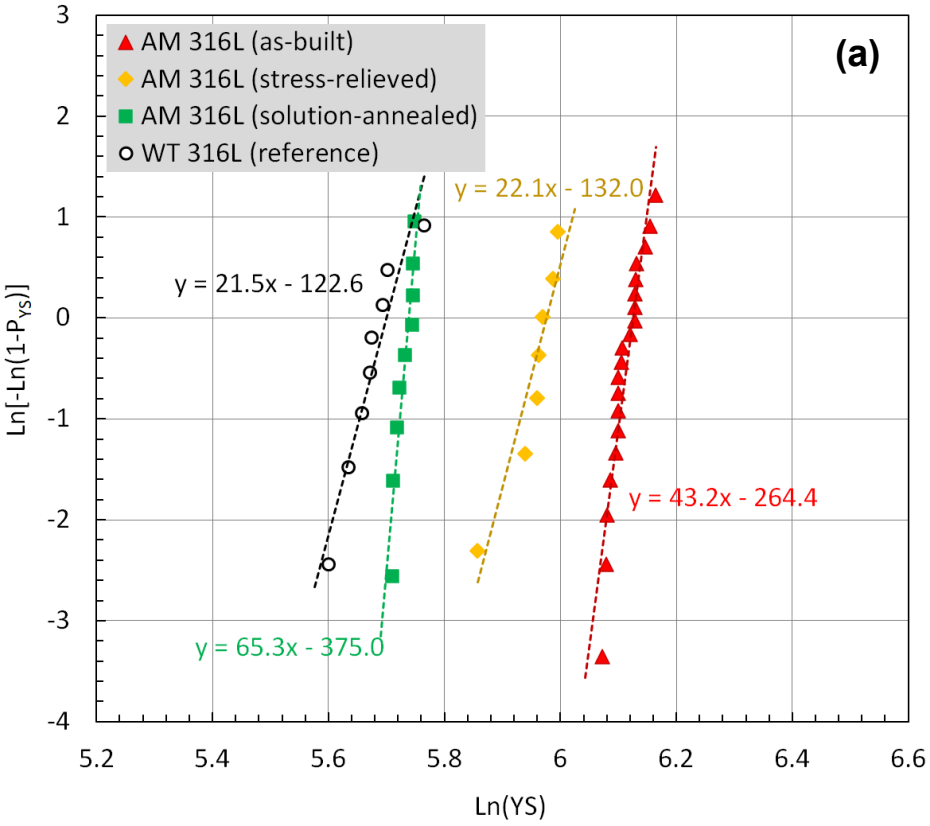


**Figure 7. Weibull plots for (a) YS data and (b) TE data of 316L SSs in four different conditions.**

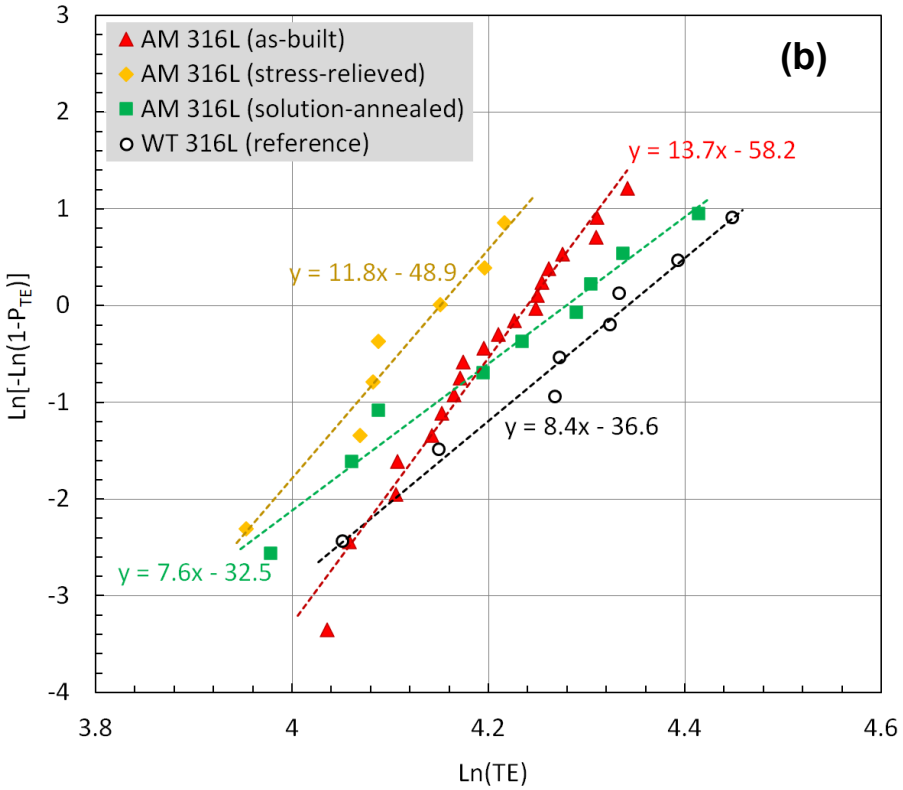


Figure 7. (continued)

### 3.4. Spatial Distribution of Strength in AM 316L Build

This section will discuss the spatial distribution of tensile properties data for the two 40 mm cube parts 11 and 21 of the 20201119 build in the form of property contour maps. A table that contains the mean property and standard deviation (σ) values is included with each set of property contour maps. The tensile property data from two layers in the cubic parts from the middle ($z$ = 14 mm) and near-top ($z$ = 31 mm) layer are mapped onto the $x$-$y$ plane by creating contour lines via second-order data regression curves. As discussed in Section 2.2, the locations of the cubes likely affected their mechanical properties, which could have been caused by multiple factors in the 3D printing process, including: (1) the cooling rates of melting pools are higher in the interior locations surrounded by a more highly conductive metallic body; (2) the differences in proximity to other parts, as well as the inert gas inlet of the 3D printer, would have influenced their convective cooling and thus their mechanical properties; and (3) variations in other printing and postbuild treatment conditions are possible, such as input laser power, properties of metal powder, and temperature distribution in stress-relieving treatments. Figures 8 and 9 show the contour plots for the 0.2% offset YS of parts 11 and 21. The average YS for both parts is high, and the intra- and inter-part variation is relatively low. However, there is a slight YS increase at the $y$ = 0 mm and $y$ = 40 mm faces relative to the interior of the part, likely due to the differences in cooling rates between the faces and the interior. This is not observed at the $x$ = 0 mm and $x$ = 40 mm faces, likely due to the orientation of the SS-J3 samples because the major faces of each specimen are normal to the $y$-axis. The deforming region (i.e., gage section) of these specimens is several millimeters away from the surface. If this dataset were more complete and had more variation in specimen orientation, a relatively high YS would likely be observed around the perimeter of the part, which would give way to a relatively low YS region in the interior. Although the patterns of YS distributions are different depending on the $z$-position and part number, similar mean YS and standard deviation values are measured for the two $z$-locations.

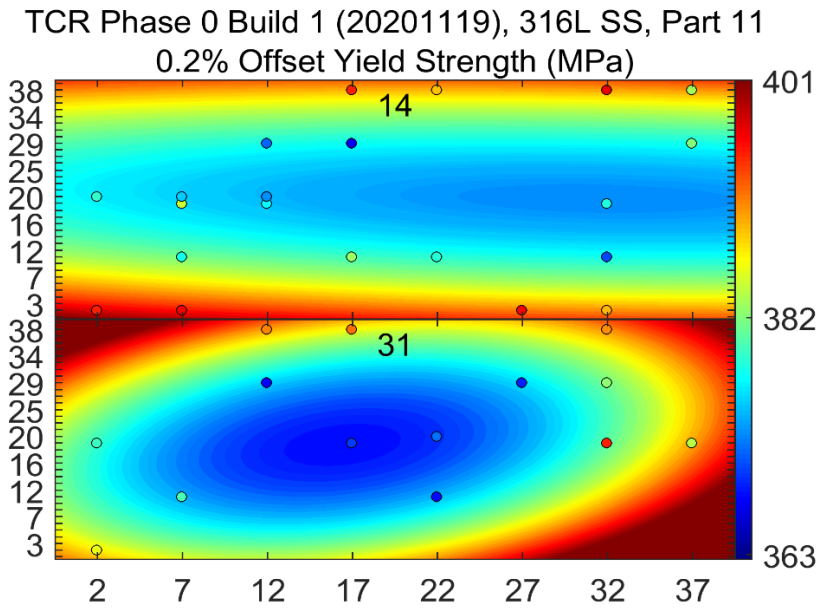


| *Z* (mm) | Mean YS (MPa) | Standard deviation (MPa) |
|---|---|---|
| 14 | 382.8 | 9.46 |
| 31 | 380.4 | 9.98 |
| Overall | 381.8 | 9.59 |

**Figure 8. YS contour plots for the two layers of part 11: $z$ = 14 mm (top) and 31 mm (bottom).**

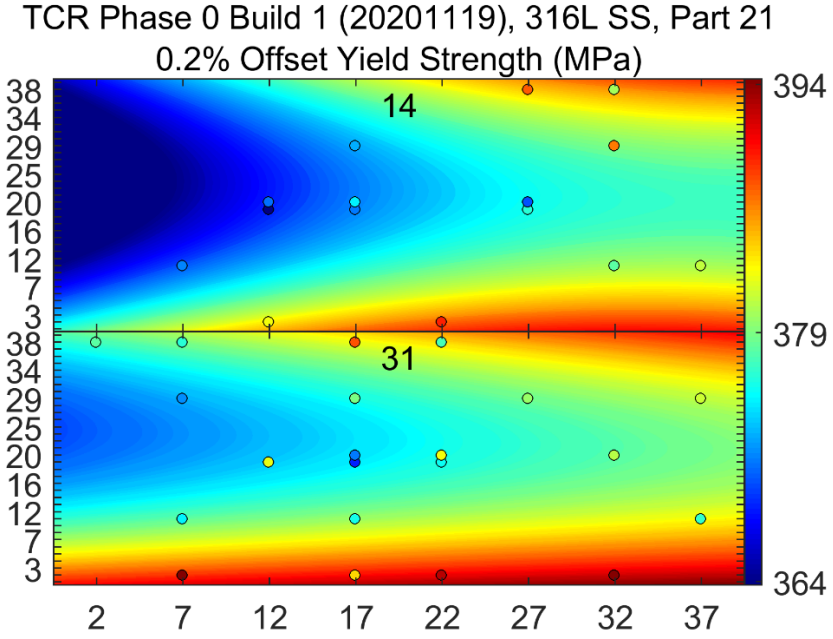


| *Z* (mm) | Mean YS (MPa) | Standard deviation (MPa) |
|---|---|---|
| 14 | 377.1 | 7.55 |
| 31 | 380.4 | 7.57 |
| Overall | 379.1 | 7.63 |

**Figure 9. YS contour plots for the two layers of part 21: $z$ = 14 mm (top) and 31 mm (bottom).**

Figures 10 and 11 show contour plots for the UTS of parts 11 and 21. Again, the contours shown are second order in both the *x*- and *y*-direction because reliable higher order contours require more data points than what is available. Although only a fraction of the samples machined from each part (576 specimens per part) were tested, insight into the properties can be obtained from this small sample population. Overall, both parts show excellent strength and low regional variation, and the standard deviation in UTS was less than 8 MPa for each part. The contour plots indicate that for part 21, there is a somewhat noticeable gradient in UTS from the (0,40,14) mm region to the (32.5,0,31) mm region. However, because samples were not tested near the (0,40,14) mm region, it is difficult to determine whether this reflects the actual part properties or whether this is a result of the extrapolatory nature of the contour plot.

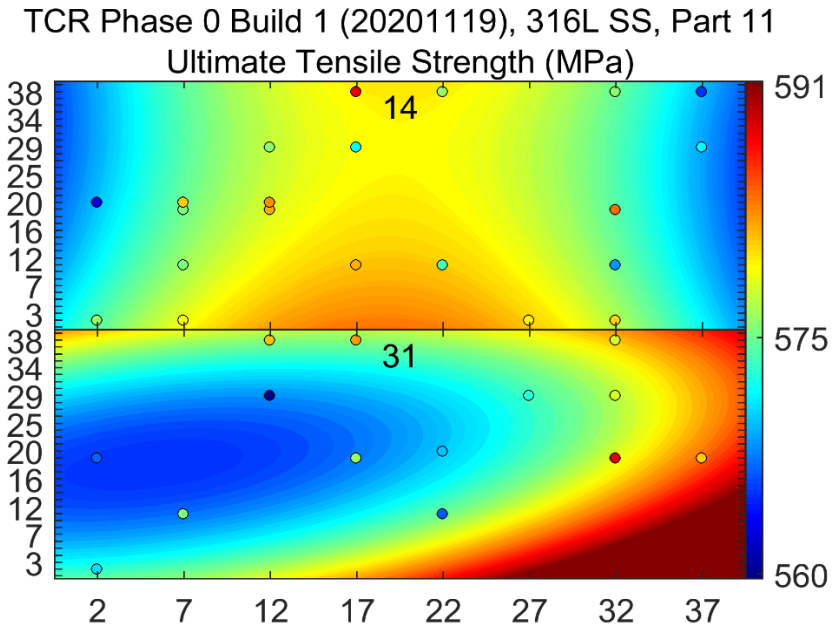


| *Z* (mm) | Mean UTS (MPa) | Standard deviation (MPa) |
|---|---|---|
| 14 | 576.5 | 6.26 |
| 31 | 574.0 | 9.90 |
| Overall | 575.5 | 7.88 |

**Figure 10. UTS contour plot for part 11: $z$ = 14 mm (top) and 31 mm (bottom).**

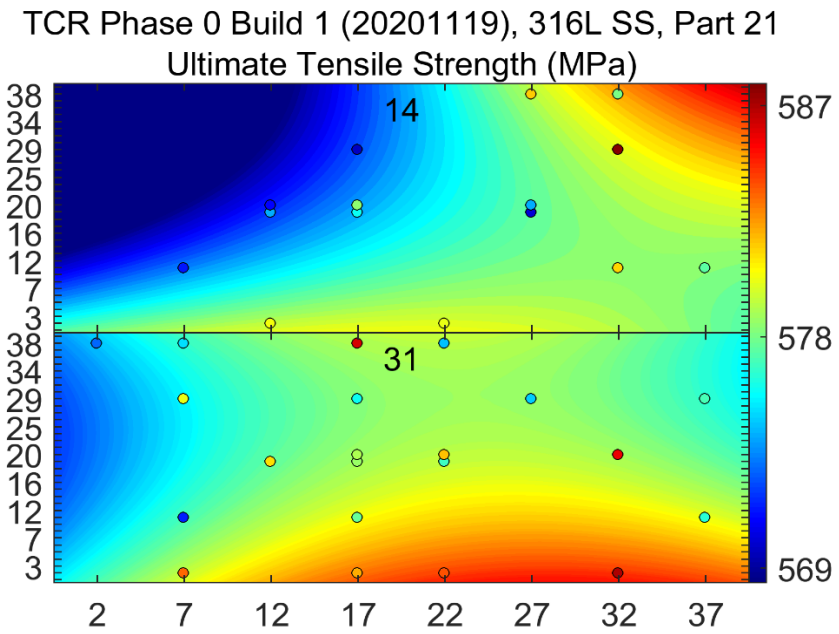


| *Z* (mm) | Mean UTS (MPa) | Standard deviation (MPa) |
|---|---|---|
| 14 | 576.8 | 5.19 |
| 31 | 579.1 | 4.47 |
| Overall | 578.1 | 4.85 |

**Figure 11. UTS contour plots for part 21: $z$ = 14 mm (top) and 31 mm (bottom).**

### 3.5. Spatial Distribution of Ductility in AM 316L Build

Figures 12–15 show the UE and TE contour plots for parts 11 and 21. As expected, the UE and TE show similar magnitudes of location dependence for each part, although the location dependencies between the two parts are very different. For part 11, the UE and TE at a height of 31 mm show a location dependence similar to the UTS and YS at the same height, indicating proportionality between strength and ductility in that particular region. This proportionality relationship between strength and ductility might originate from the variation of cooling rates that control the fineness of the microstructure. Producing finer microstructures can simultaneously improve the strength and ductility of the alloy. For part 21, there is a loose correlation between regions of higher strength and lower ductility, and vice versa. More typical strengthening mechanisms, such as those that depend on dislocation density and precipitation amount, are dominant, which generally leads to an inverse strength-ductility relationship. Despite these explanations, the specific mechanism that governs the strength and ductility distributions is often unclear and might be too complex to determine a clear relationship between them. As indicated in Section 3.5, the particular heat treatment used for this build might be insufficient to erase all extra features from the AM process; however, it might create transitional microstructures, which could be sensitive to small variations in various conditions. The effect of the heat treatment on the formation and growth of other phases is also unclear. Without additional mechanical and microstructural investigations, the assertions are largely conjectural.

Overall, the standard deviations (σ) in strength (i.e., YS and UTS) data are quite small (<3%), whereas the those in ductility (i.e., UE and TE) are much higher (3< σ <16.1%). Similar differences between the variabilities of strength and ductility are also observed in the Weibull analysis, as shown in Figures 7(a) and 7(b), in which the UE data have a much smaller Weibull modulus or larger variability. This is a general characteristic of metallic materials.

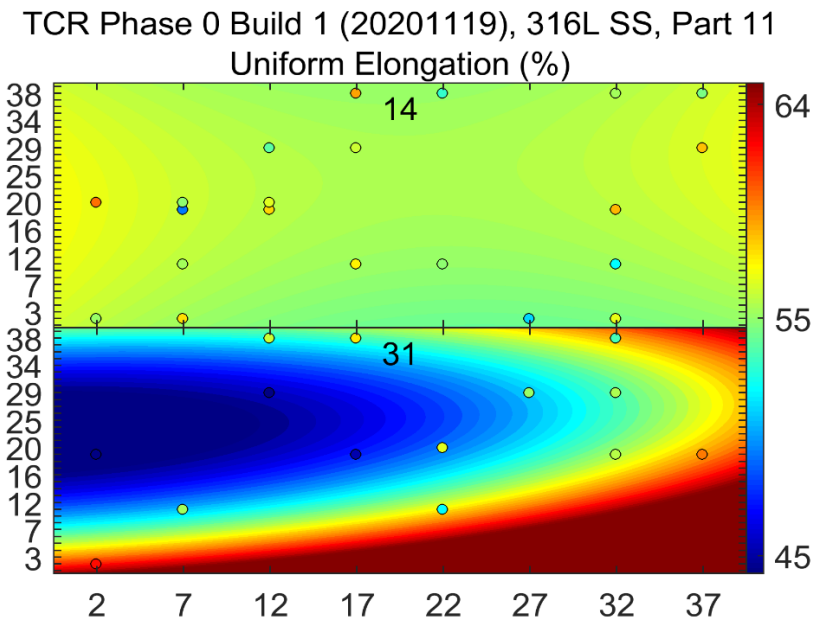


| *Z* (mm) | Mean UE (%) | Standard deviation (%) |
|---|---|---|
| 14 | 55.6 | 2.72 |
| 31 | 53.0 | 7.34 |
| Overall | 54.6 | 5.16 |

**Figure 12. UE contour plots for part 11: $z$ = 14 mm (top) and 31 mm (bottom).**

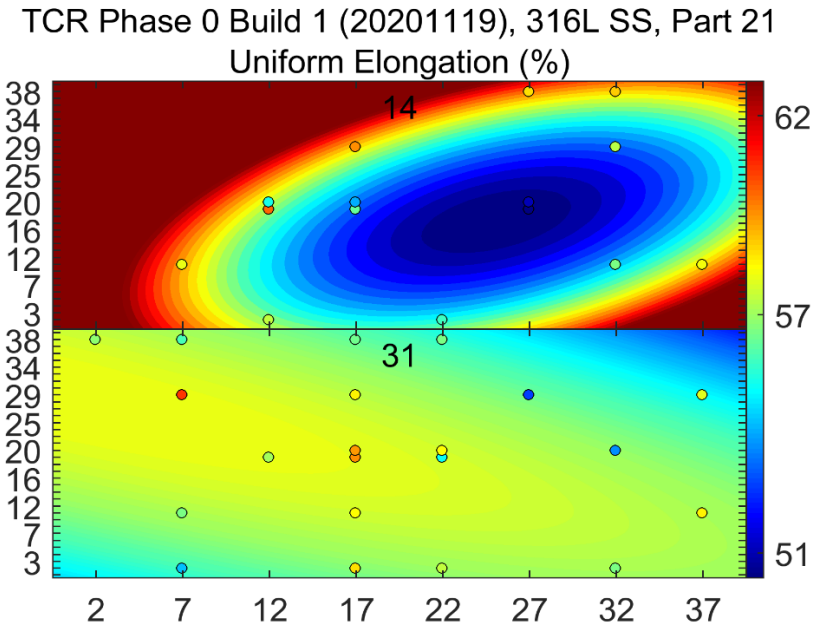


| *Z* (mm) | Mean UE (%) | Standard deviation (%) |
|---|---|---|
| 14 | 56.0 | 4.26 |
| 31 | 57.1 | 1.96 |
| Overall | 56.6 | 3.12 |

**Figure 13. UE contour plots for part 21: $z$ = 14 mm (top) and 31 mm (bottom).**

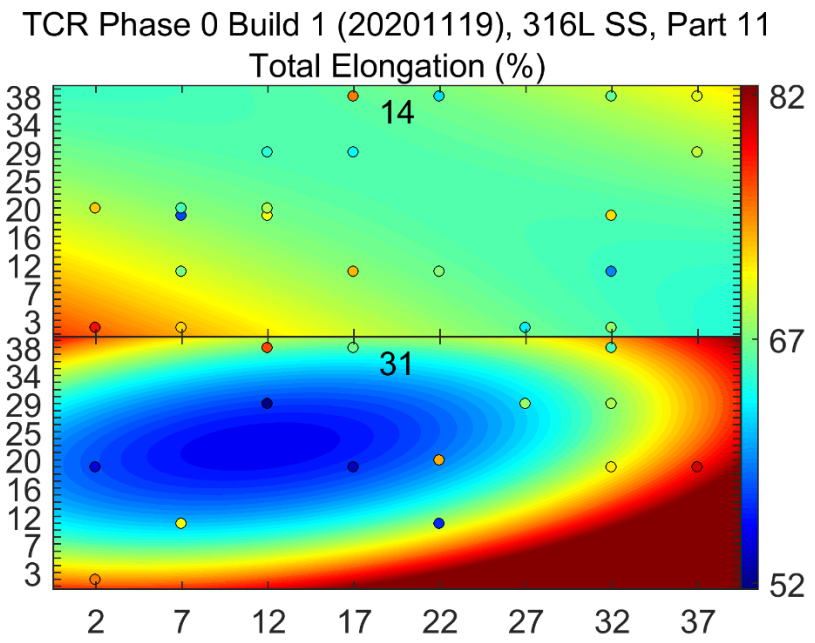


| *Z* (mm) | Mean TE (%) | Standard deviation (%) |
|---|---|---|
| 14 | 67.9 | 5.15 |
| 31 | 66.0 | 10.63 |
| Overall | 67.1 | 7.73 |

**Figure 14. TE contour plots for part 11: $z$ = 14 mm (top) and 31 mm (bottom).**

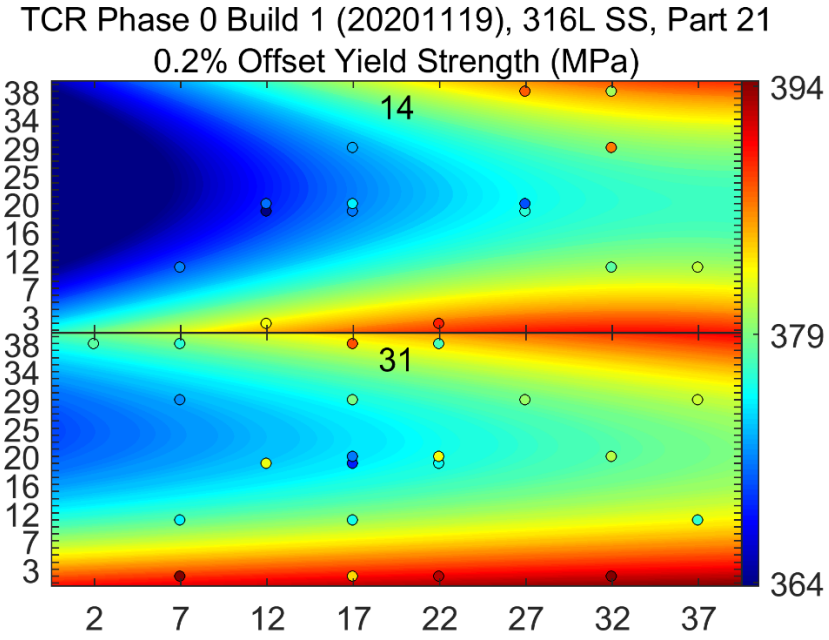


| *Z* (mm) | Mean TE (%) | Standard deviation (%) |
|---|---|---|
| 14 | 69.1 | 7.98 |
| 31 | 69.4 | 4.79 |
| Overall | 69.3 | 6.21 |

**Figure 15. TE contour plots for part 21: $z$ = 14 mm (top) and 31 mm (bottom).**

# 4. POSTIRRADIATION PROPERTIES

The 316L SSs with four different initial microstructures are expected to respond differently to the elevated and high-temperature (~300°C and ~600°C) neutron irradiations. Particularly, starkly different irradiation temperature dependencies in their tensile deformation behavior are expected because of the significantly different initial strengths of those microstructures. Uniaxial tensile curves and engineering property data are presented in Sections 4.1 and 4.2, respectively, for 0.2 and 2 dpa specimens. The following sections elucidate the substantially different tensile deformation behaviors of the 316L materials: (1) after low-temperature (~300°C) and high-temperature (~600°C) irradiations and (2) with high-strength (as-built and stress-relieved AM 316L) and low-strength (solution-annealed AM 316L and WT 316L) microstructures.

## 4.1. Stress-Strain Behavior after Irradiation to 0.2 dpa

Figures 16 and 17 show the effects of a low-dose (0.2 dpa) neutron irradiation on the stress-strain behavior of the four 316L steels. Two sets of engineering stress-strain curves are compared in the respective figures for the effects of low- and high-temperature irradiations. Furthermore, the full set of the engineering tensile property parameters (i.e., YS, UTS, UE, and TE) obtained from the stress-strain curves is presented.

In steels, reactor irradiation below 400°C retains a high density of radiation-produced defect clusters, and the typical irradiation effects of a significant increase in strength (i.e., hardening) and a reduction in ductility are observed in mechanical testing. Figure 16 shows the typical radiation effects after irradiation at 260°C. In Figure 16, the stress-strain curves obtained at 260°C after irradiation are compared with the curves obtained at 300°C before irradiation, which means that the actual radiation-induced changes are slightly less significant when compared with the baseline data obtained at 260°C. In Figure 16, the WT 316L steel, which has the lowest initial strength among the four materials, shows significant irradiation hardening and ductility reduction after the 260°C irradiation (dotted gray curve vs. solid gray curve). Although this alloy is significantly hardened by the low dose (0.2 dpa) irradiation, particularly around the yield point, its ductility reduction is relatively moderate, and it still retains a high TE (~30%). The AM 316L alloys in three different initial conditions with relatively higher strengths show degrees of irradiation hardening and ductility reduction similar to the WT 316L. Both strong materials—AM 316L in the as-built and stress-relieved conditions—show a relatively smaller percent change in strength after the 260°C irradiation.

In Figure 17, the tensile curves after higher temperature (690°C) irradiation show starkly different behaviors from the baseline test curves. The stress-strain curves in all four process conditions show commonly lowered strength and increased elongation after irradiation—which are usually referred to as *irradiation softening* and *radiation-induced ductilization (RIDU)*, respectively [43]—and are found in high-temperature (>400–500°C for steels) irradiations. This phenomenon is primarily due to the rapid thermal annihilation of radiation-produced point defects and might be more accelerated in the high-strength microstructures of alloys with incomplete stress relaxation, such as the as-built and stress-relieved AM 316L steels. In Figure 17, these two higher strength 316L steels show a more significant reduction of strength compared with the softer, fully annealed materials. In these fully annealed alloys, the radiation-induced decrease of strength becomes more obvious with increasing strain as the annihilation of deformation-produced dislocations become more significant in higher strain regions. However, the radiation effect on tensile behavior is not substantial at such high irradiation and test temperatures.

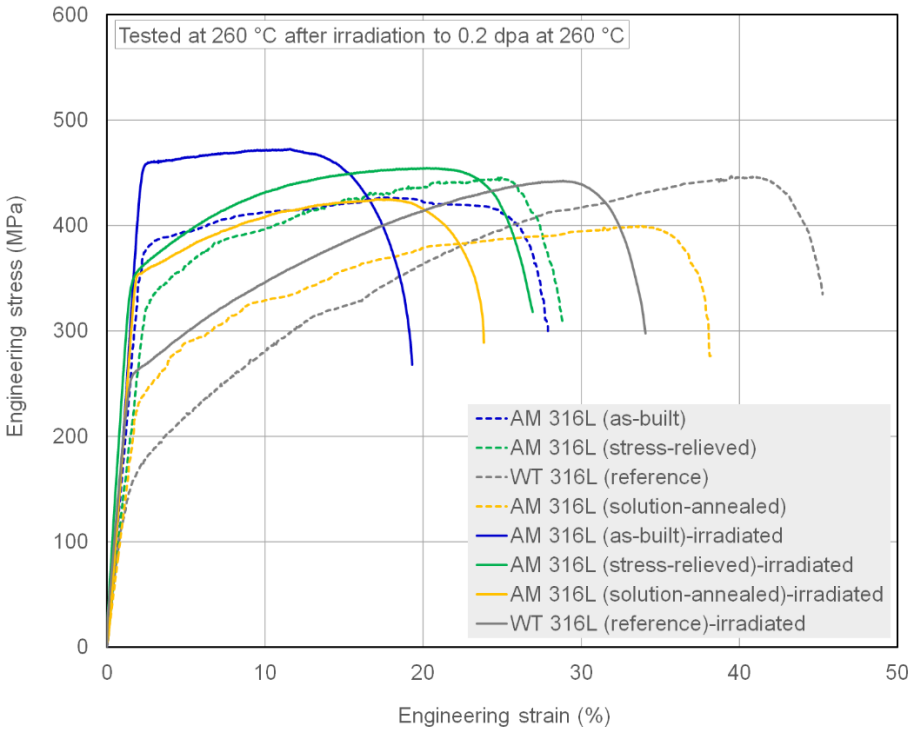


**Figure 16. Engineering stress-strain curves of AM 316L in the as-built, stress-relieved, and solution-annealed conditions and WT 316L tested at 260°C after irradiation to 0.2 dpa at 260°C (solid lines), which are compared with those of nonirradiated materials tested at 300°C (dotted lines).**

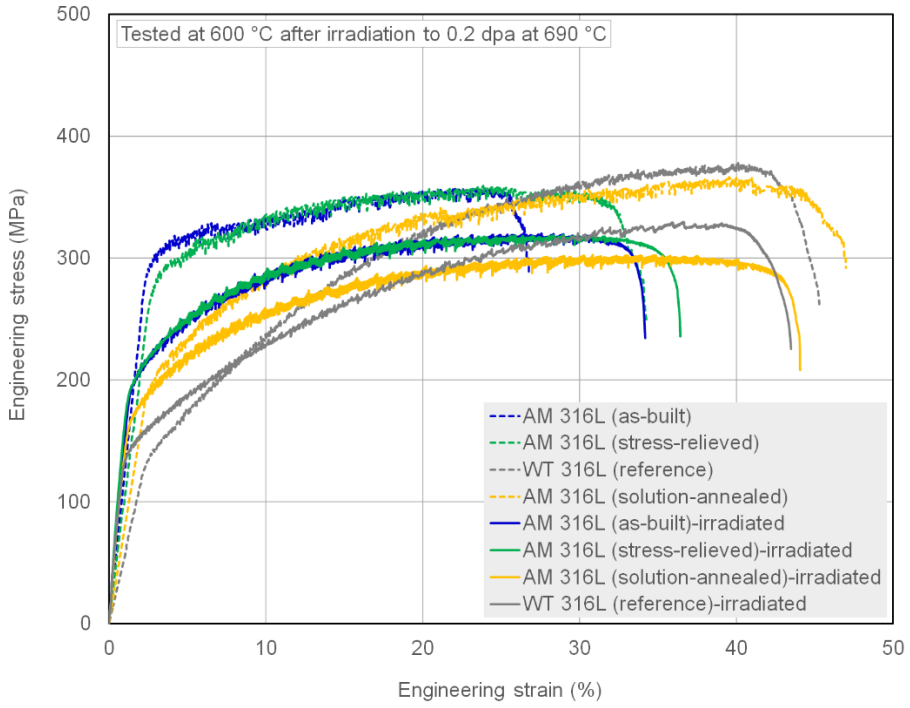


**Figure 17. Engineering stress-strain curves of AM 316L in the as-built, stress-relieved, and solution-annealed conditions and WT 316L tested at 600°C after irradiation to 0.2 dpa at 690°C (solid lines), which are compared with those of nonirradiated materials tested at 600°C (dotted lines).**

### 4.2. Engineering Tensile Properties after Irradiation to 0.2 dpa

Figures 18 and 19 compare the tensile property parameters of the WT and AM 316L SSs determined from the stress-strain curve data, including those shown in Figures 16 and 17. The measurements of strength (i.e., YS and UTS) and ductility (i.e., UE and TE) parameters for the four 316L SSs are compared in eight testing and irradiation conditions before and after irradiation to 0.2 dpa. In Figure 18(a), comparing the YS datasets for irradiated materials with those of nonirradiated materials consistently shows that in all four process conditions, the 260°C irradiation increases YS but the 690°C irradiation decreases YS. Also, the relatively softer materials (stress-relieved AM 316L and WT 316L) display only small changes in YS after irradiation at 690°C.

On the other hand, the radiation effects on UTS are similar to the effects on YS, although their irradiation-induced changes are smaller, as shown in Figure 18(b). The RT data particularly show a slight decrease after both low- and high-temperature irradiations, except for the WT 316L, which shows significant irradiation hardening. Typically, the YS represents the strength of an alloy in early plastic deformation and should be sensitive to the defect density and distribution in microstructure. One of the most influential factors in YS change is the irradiation temperature because it can determine the density and size of surviving defects and processing of initial microstructures [44]. The UTS values, which are measured at relatively higher strains or are later part of deformation, show relatively smaller changes after irradiation compared with the irradiation-induced changes in YS. This might be because the total amounts of radiation- and deformation-induced defects contained in the same alloy microstructures can become closer to a saturated amount at high strain levels, leading to mostly similar strengths.

Radiation generally has opposite effects on ductility and strength. Figure 19 summarizes the ductility data (i.e., UE and TE) of the four 316L materials after irradiation to 0.2 dpa. Figure 19(a) shows mostly a decrease in UE after irradiation at 260°C and an increase in UE after irradiation at 690°C. Only a few exceptions deviated from this trend, including the slight decreases of UEs at RT in the stress-relieved AM 316L, at 300°C and at 600°C in the solution-annealed AM 316L, all after irradiation at 690°C. Radiation also affects TE similarly to UE. Figure 19(b) generally shows a decreases in UE after irradiation at 260°C and an increase after irradiation at 690°C, except for some opposite effects. Some exceptions include the slight decrease of TE in the stress-relieved AM 316L and as-built AM 316L irradiated at 690°C and tested at RT, as well as the solution-annealed AM 316L irradiated at 260°C and tested at RT. As observed in the UTS comparison, the differences among the radiation-induced TE changes of four different 316L materials are generally insignificant when compared in the same irradiation condition.

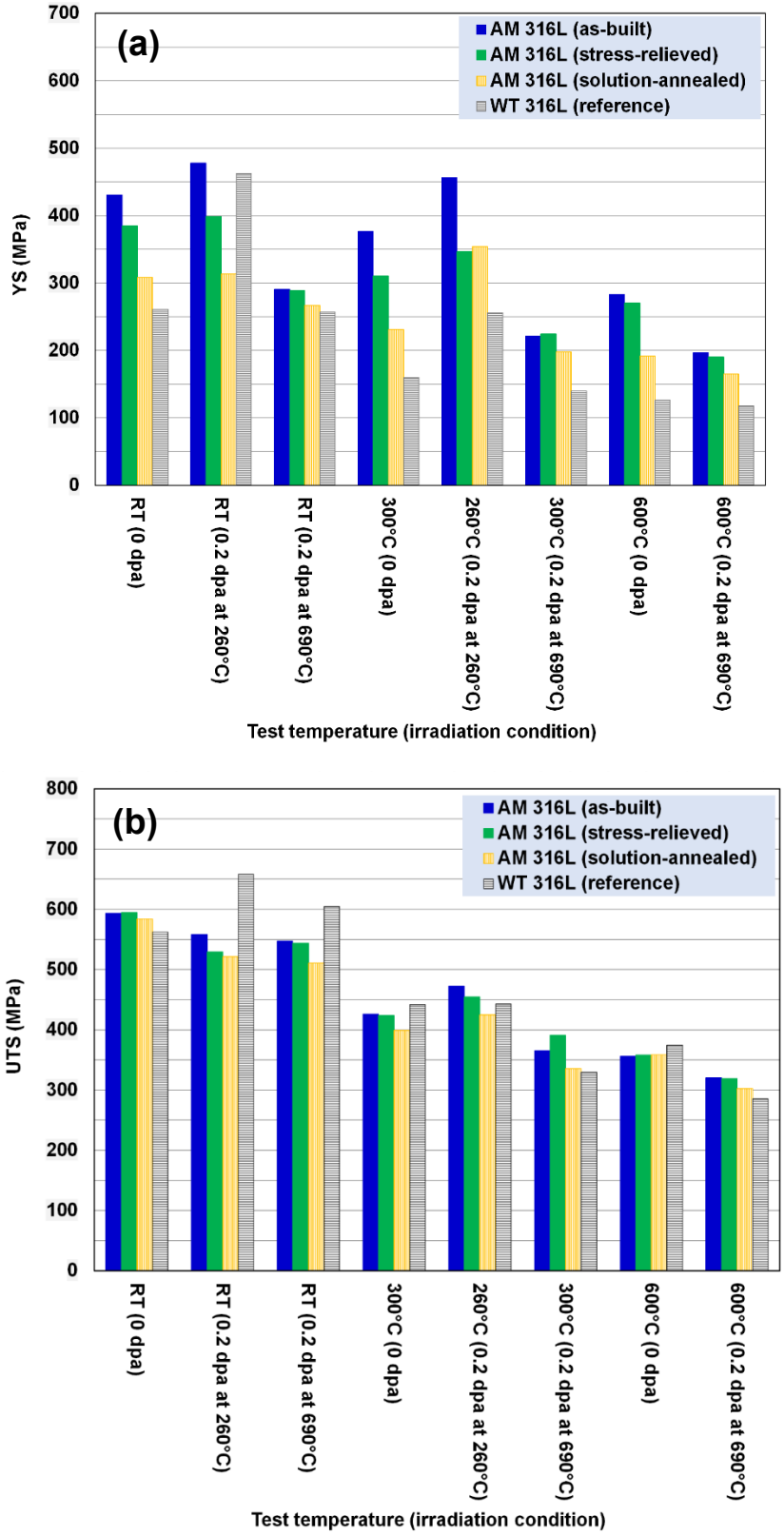


**Figure 18. Comparison of tensile strength data for the AM and WT 316L SSs after irradiation to 0.2 dpa: (a) YS and (b) UTS in various irradiation and test conditions.**

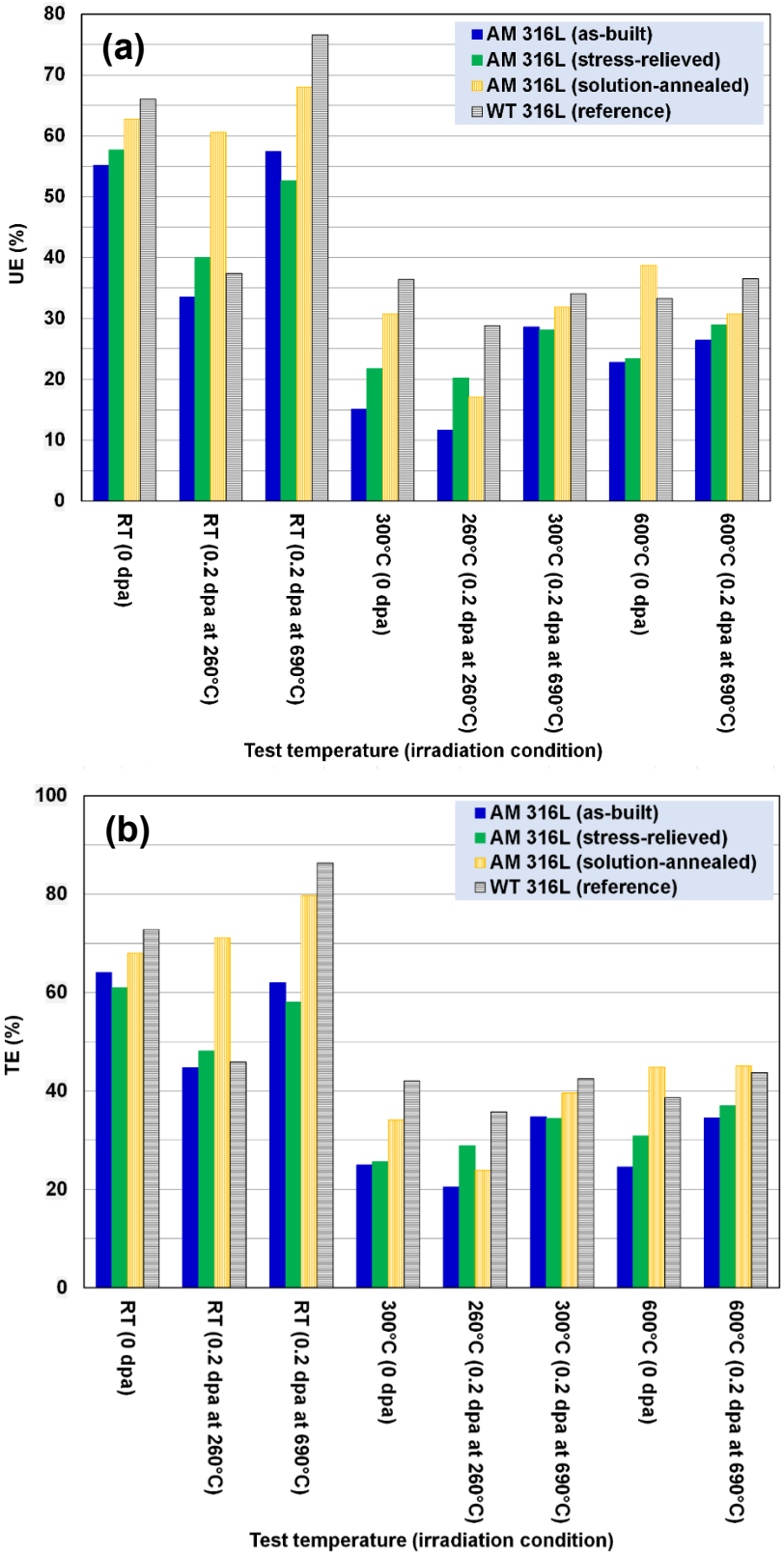


**Figure 19. Comparison of tensile strength data for the AM and WT 316L SSs after irradiation to 0.2 dpa: (a) UE and (b) TE in various irradiation and test conditions.**

### 4.3. Stress-Strain Behavior after Irradiation to 2 dpa

As expected, the AM and WT 316L SSs responded more strongly to the neutron irradiation at the higher dose of 2 dpa than to the light irradiation to 0.2 dpa. Figures 20–23 present the effects of irradiation on the stress-strain behavior of the four 316L steels in selected testing and irradiation conditions. The collections of engineering stress-strain curves from the RT, 300°C, 500°C, and 600°C tensile tests are compared in Figures 20–Figure 23, respectively, in which the stress-strain curves of four 316L steels after irradiation are compared with corresponding curves before irradiation.

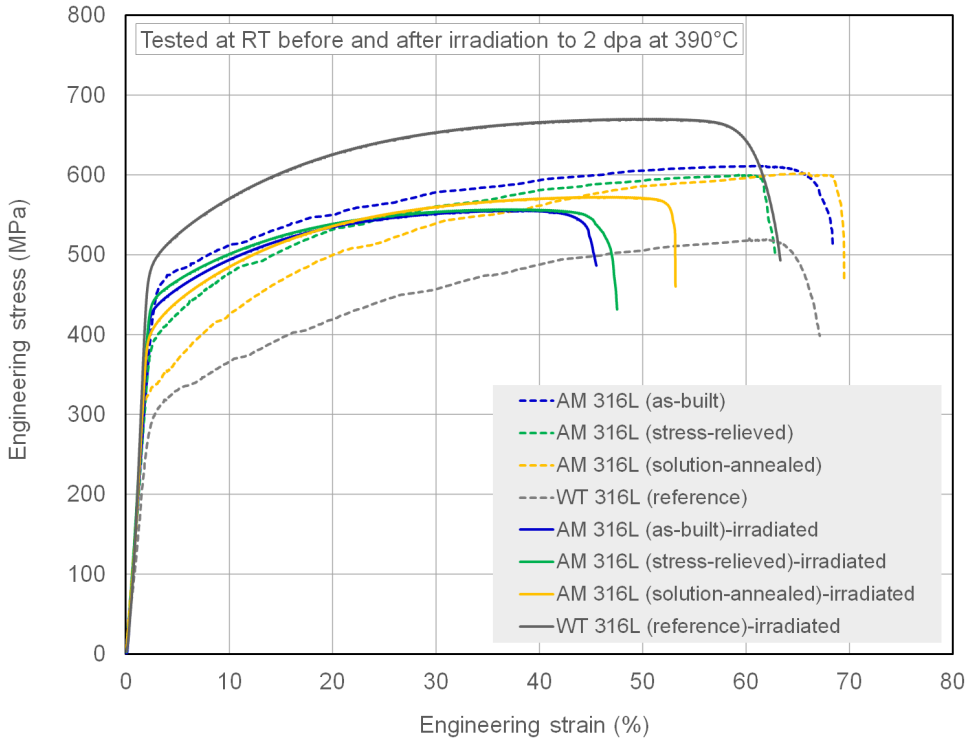


**Figure 20. Engineering stress-strain curves of AM 316L in as-built, stress-relieved, and solution-annealed conditions and WT 316L tested at RT after irradiation to 2 dpa at 390°C. Dotted lines indicate nonirradiated materials, and solid lines indicate materials after irradiation.**

In the RT test curves in Figure 20, the WT 316L steel with the lowest initial strength among the four materials demonstrates the highest irradiation hardening after the 390°C irradiation (dotted gray curve vs. solid gray curve). Although is the most irradiation-hardened alloy among those studied, its ductility reduction is relatively moderate after irradiation at elevated temperature. On the other hand, the AM 316L alloys show less irradiation hardening but a more significant ductility reduction when compared with the WT 316L. Among these AM 316L SSs in three different conditions, the softest solution-annealed AM 316L experienced nontrivial irradiation hardening but in the relatively early deformation only. Both strong materials—AM 316L steels in the as-built and stress-relieved conditions—show relatively small strength changes after irradiation at 390°C. At this temperature, the amount of ductility loss is inversely proportional to the initial alloy strength. The largest ductility reduction (>30% narrowed elongation range of stress-strain curve) was found in the as-built 316L; the other two AM 316L steels lost less significant amounts of ductility during irradiation.

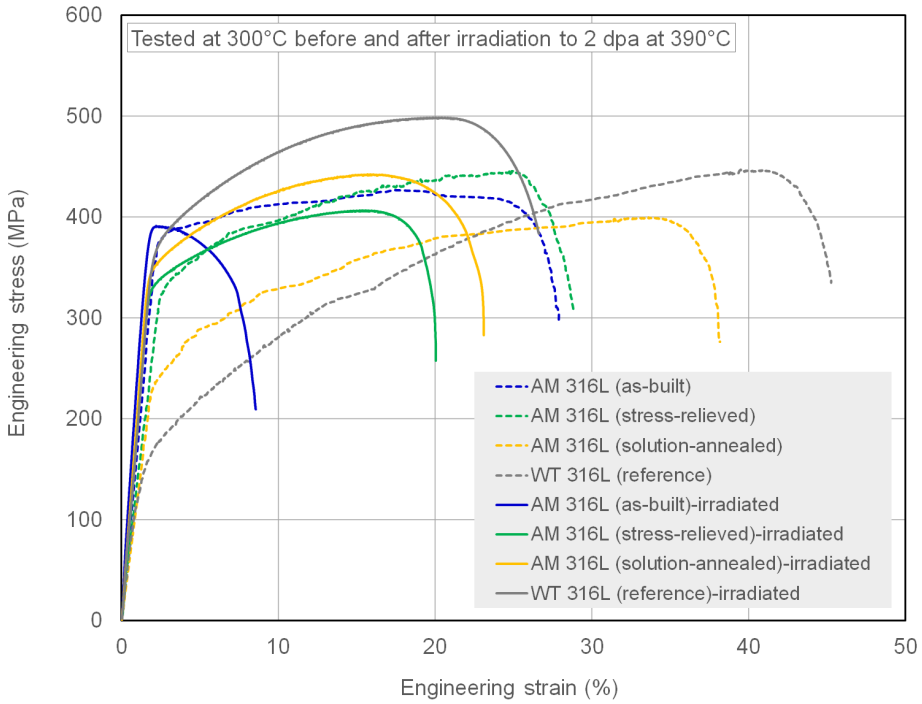


**Figure 21. Engineering stress-strain curves of AM 316L in as-built, stress-relieved, and solution-annealed conditions and WT 316L tested at 300°C after irradiation to 2 dpa at 390°C. Dotted lines indicate nonirradiated materials, and solid lines indicate materials after irradiation.**

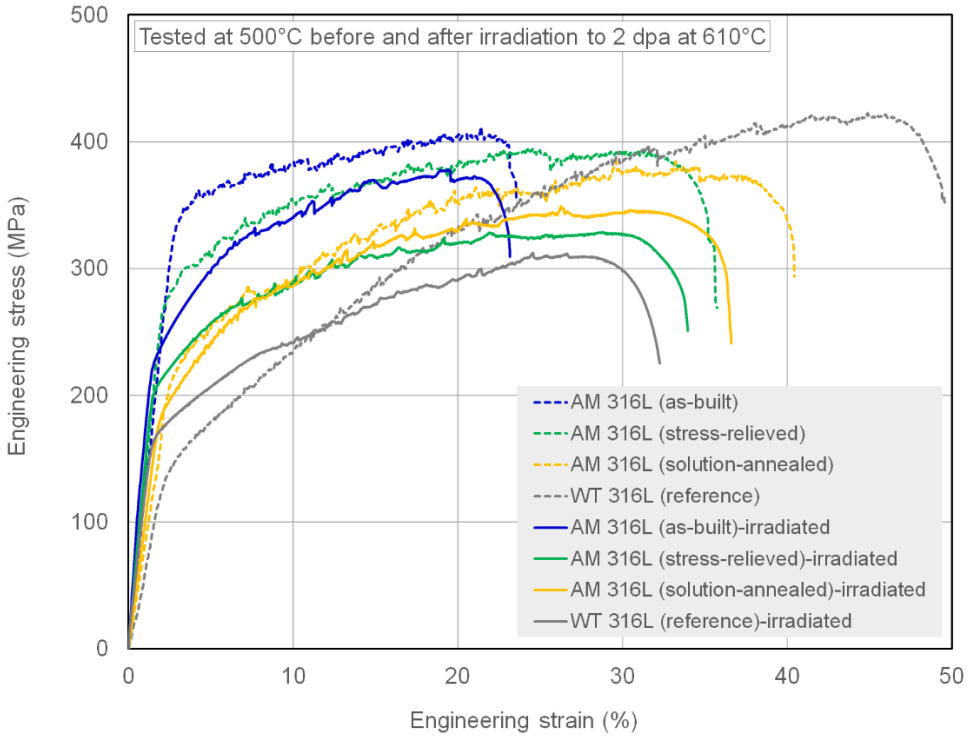


**Figure 22. Engineering stress-strain curves of AM 316L in as-built, stress-relieved, and solution-annealed conditions and WT 316L tested at 500°C after irradiation to 2 dpa at 610°C. Dotted lines indicate nonirradiated materials, and solid lines indicate materials after irradiation.**

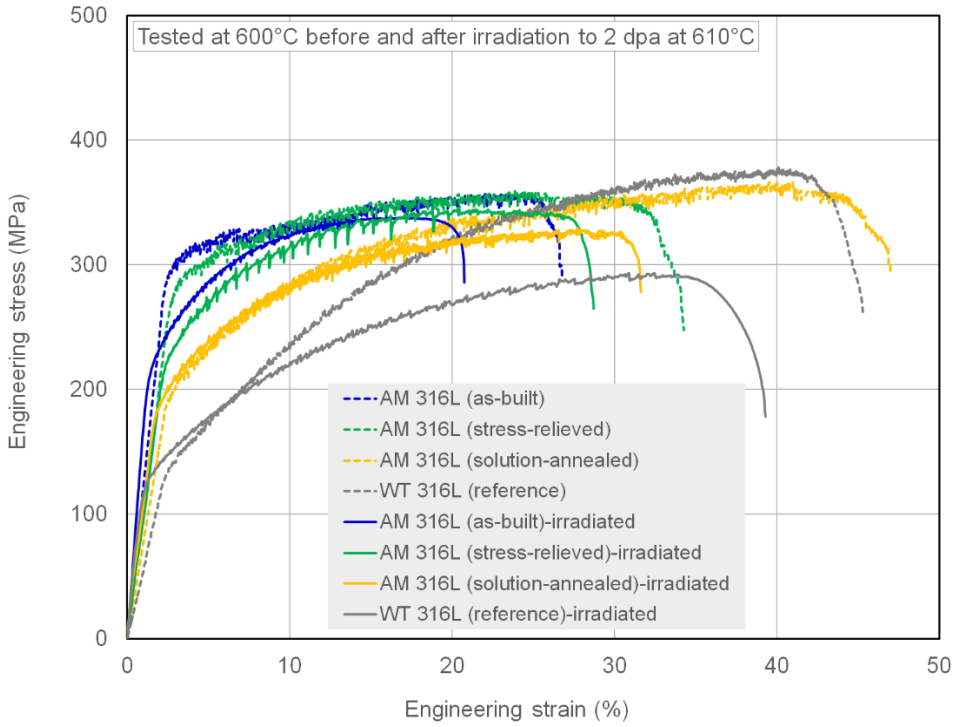


**Figure 23. Engineering stress-strain curves of AM 316L in as-built, stress-relieved, and solution annealed conditions and WT 316L tested at 600°C after irradiation to 2 dpa at 610°C.**

One aspect that can explain the tensile behaviors at RT is the characteristic deformation of low-stacking fault energy alloys, such as the 316L SSs [45,46]. In these alloys, gliding dislocations tend to be separated into partial dislocations under high stress, which leads to more linear glides and thus a higher, more sustainable work hardening [46-49]. Therefore, the significantly higher strength measured in early deformation of the AM 316L alloy does not result in reduced ductility at RT. This positive effect from the strength-enhanced linear glides tends to diminish at higher temperatures because the overall strength of the alloy is reduced, so the dislocation glides become more random (i.e., less linear). This effect becomes evident in the 300°C tensile testing for both irradiated and nonirradiated materials; the strength and elongation ranges of the stress-strain curves shown in Figure 21 are significantly reduced from those displayed in Figure 20. Irradiation hardening behaviors due to the 390°C irradiation are similarly measured at RT and 300°C; however, the reduced strain-hardening capability at 300°C caused the 316L materials to respond more sensitively to the irradiation, so the irradiation-induced ductility loss is more significant. As an extreme example, the AM 316L in the as-built condition with the highest strength in the low-strain range displays a prompt necking immediately after yield. Furthermore, compared with the radiation effect in the RT testing, the WT 316L SS in 300°C tests experienced a much larger ductility reduction after the same 390°C irradiation.

Figure 22 compares the tensile stress-strain curves obtained at 500°C after irradiation to 2 dpa at 610°C. The pattern of irradiation-induced hardening and ductility reduction observed at lower test temperatures is not observed at this temperature. The details of the irradiation effects are significantly different. In WT 316L SS, the irradiation hardening that occurs in the low-strain range becomes irradiation softening in the higher strain range, and the same is observed in the stress-relieved 316L in the 300°C tests (Figure 21). Except for the low elongation range of the two solution-annealed WT and AM 316L SSs, the stress-strain curves were lowered by irradiation, which indicates that irradiation softening is common in these irradiation and test temperatures [43]. Contrary to the tensile curves from 300°C testing, the loss of

ductility after irradiation is not significant, except in the WT 316L for which initial strength is much lower than the AM 316L steels in the three conditions. Although none was substantial, the ductility loss after irradiation was also more significant in the softer materials: the WT 316L loses the most (almost 20%) total ductility, and the AM 316L (solution-annealed) loses the next largest amount, and so on.

As shown in Figure 23, the effects of irradiation at 610°C on stress-strain behavior measured at 600°C are not significantly different from those measured at 500°C; however, the radiation-induced changes are slightly more significant at this higher temperature. Figure 23 compares the tensile stress-strain curves obtained at 600°C after irradiation to 2 dpa at 610°C. Irradiation softening was observed in all materials, except for the low-strain region of the two lower strength materials (AM 316L and WT 316L in the solution-annealed condition). Again, contrary to the tensile curves from the 300°C test, the loss of ductility after irradiation is not significant, except in the WT 316L for which initial strength is much lower than the AM 316L steels in the three conditions.

Overall, irradiation softening and ductility loss are relatively moderate at high temperatures (500 and 600°C) after irradiation at 610°C, and no extreme case, such as embrittlement or prompt necking at yield, is observed. This might be because the effective defect annihilation at such a high temperature (610°C) limited the irradiation hardening amount and thus maintained ductility.

### 4.4. Engineering Tensile Properties after Irradiation to 2 dpa

This section discusses the effect of the testing and irradiation conditions on the engineering tensile properties. Figures 24 and 25 show the tensile property parameters of the WT and AM 316L SSs determined from the stress-strain data. Each strength (YS and UTS) and ductility (UE and TE) parameter for the four 316L SSs is compared in 12 different testing and irradiation conditions; this demonstrates a variety of mechanical behaviors, depending on irradiation, initial microstructure, and test conditions.

Typically, YS represents the strength of a material in early plastic deformation and should be highly sensitive to the defect density and distribution in the microstructure before deformation. One of the most influential factors in YS change is the irradiation temperature because it can determine the density and size of surviving defects and processing of initial microstructures [44]. Figure 24(a) shows that the lower temperature (390°C) irradiation increases YS in both solution-annealed 316L steels (AM 316L solution-annealed and WT 316L), and it can either increase or decrease YS in the stronger AM 316L steels. After irradiation at 390°C, for example, the AM 316L in the as-built condition showed YS increases in the 300 and 390°C tests, and the same alloy showed slight irradiation softening at RT. After irradiation at 610°C, all the AM 316L materials showed 29–190 MPa YS decreases, regardless of different test temperatures. However, this tendency for irradiation softening was not shown by the WT 316L SS, which showed a >200 MPa YS increase when tested at 300 and 500°C.

As discussed in Section 4.3, the UTS data have much smaller variation among the WT 316L and AM 316L alloys than their YS data. Similarly, the variation of UTS among the 316L alloys is relatively smaller after irradiation, as shown in Figure 24(b). This confirms the earlier observation that UTS represents the strength of the later part of deformation, and the microstructure (i.e., processing) dependence of UTS is smaller than that of YS. Another notable observation in irradiation hardening behavior is that the lowest strength alloy, WT 316L SS, shows a relatively large increase in UTS after irradiation, which is particularly obvious in the RT test data (a 25% increase in maximum) and in the 300 and 500°C test data after irradiation at 300°C. However, many of the as-built and stress-relieved AM 316L specimens experience UTS reduction after irradiation, although the softening effect measured by UTS is not significant. Overall, the test-temperature dependence of UTS is stronger than the effect of the irradiation temperature, and the radiation effect measured by UTS—either hardening or softening—is relatively insignificant.

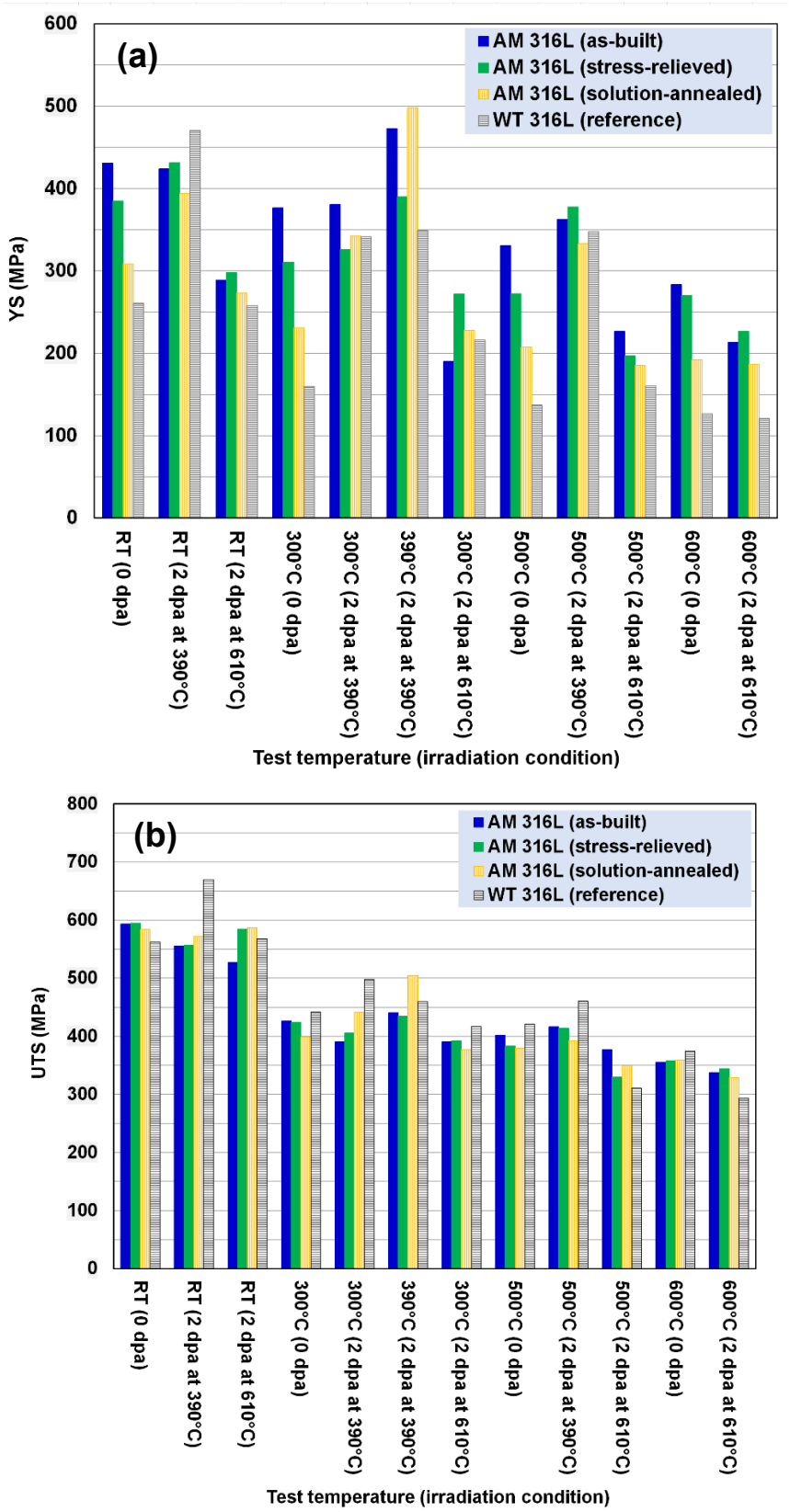


**Figure 24. Comparison of tensile ductility data for AM and WT 316L SSs after irradiation to 2 dpa: (a) YS and (b) UTS in various test and irradiation conditions.**

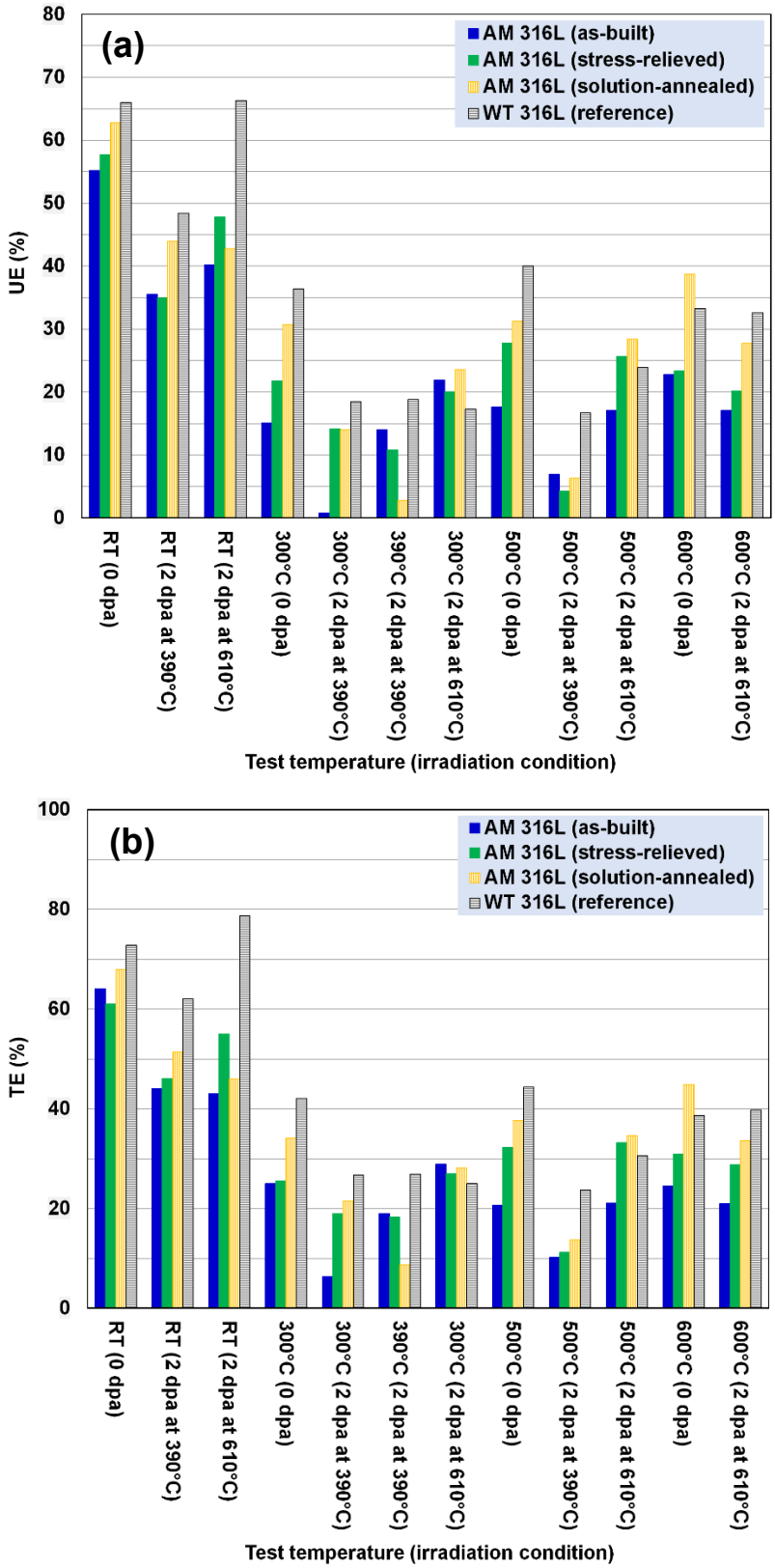


**Figure 25. Comparison of tensile ductility data for AM and WT 316L SSs after irradiation to 2 dpa: (a) UE and (b) TE in various test and irradiation conditions.**

The effect of higher dose (2 dpa) irradiation on ductility is summarized in Figures 25(a) and 25(b) for UE and TE, respectively. Among the engineering tensile parameters, UE is the parameter most sensitive to the irradiation condition; the percent increase or decrease due to the irradiation effect is the largest. All four 316L steels were observed to show ductility loss after irradiation at 390°C, whereas ductilization (i.e., a ductility increase) was demonstrated in a many cases after irradiation at 610°C. The ductility loss is generally more evident at test temperatures of 300 and 390°C than at 500 and 600°C, which Is where more ductilization cases are observed. The 500°C test data show that all three AM 316L materials have low UEs (<7%) after irradiation to 2 dpa at 390°C, which is only 20–40% of the ductility before irradiation. The most dramatic UE reduction is found in the AM 316L in the as-built condition after the lower temperature (390°C) irradiation to 2 dpa. The UE measured for this case is less than 1%, which is almost a complete loss of uniform ductility from that of ~15% before irradiation.

However, in the higher temperature (610°C) irradiation to 2 dpa, the AM 316L SSs demonstrated a respectable resilience to ductility loss. Irradiation at the higher temperature (610°C) resulted in mostly insignificant changes in ductility at the two highest test temperatures of 500 and 600°C. The relatively softer materials (WT 316L and AM 316L [solution-annealed]) demonstrated that they still can retain high ductility after irradiation at the higher temperature. A few cases demonstrated weak RIDU [43]. For example, the as-built AM 316L at 300°C and the WT 316L at RT increased their UE after the 610°C irradiation to 2 dpa. Overall, the stronger materials (AM 316L in the as-built and stress-relieved conditions) demonstrated similar or sometimes better resistance to the ductility degradation during the higher temperature (610°C) irradiation.

Figure 25(b) indicates that TE dependence on test and irradiation conditions is very similar to that of UE. This might be because all the cases tested in the research have shown ductile deformation and failure, and even if UE is very low, the necking ductility is at least more than a few percent engineering strain and is relatively consistent over the test and irradiation conditions. Furthermore, all the engineering strains measured for the necking ductility are within a range of 2 to 14% with an average of 7%, so TE can be easily estimated with reasonable accuracy if 7% is added to the UE, or vice versa. Therefore, this UE data discussion should be the same for the TE data displayed in Figure 23(b) with the exception of a few minor deviations, such as the ratios between the measured parameters.

### 4.5. Discussion on Unique Phenomena in the Deformation of AM 316L after Irradiation

As observed in the materials irradiated to 0.2 dpa, the RIDU is often observed in the as-built and stress-relieved AM 316L steels—a relatively higher strength version of the alloy—irradiated to 2 dpa at 610°C. RIDU is not obvious or does not exist at the highest test temperatures of 500 and 600°C. Some high-strength metallic materials, such as the fine-grained Mo alloy strengthened with TiC dispersoids [43] and TiAl intermetallic alloys [50], can demonstrate RIDU after high-temperature (>400°C) neutron irradiation. During high-temperature irradiation, the active migration of radiation-produced defects and alloy elements through grain boundaries and dislocation lines can enhance defect annihilation and phase precipitation and/or coarsening at boundaries, both of which can result in higher ductility [43]. Also, new twin formation during irradiation also caused a ductility increase as the twin particles grow and increase their strain-hardening capability during deformation [50]. In the AM 316L, dislocation and grain boundary densities are extraordinarily high in the as-built and stress-relieved conditions; thus, the defect annihilation at those defect sinks and the precipitation at grain boundaries from any excessive solutes should be highly active during the high-temperature (610°C) irradiation. The annihilation of existing dense dislocations, which can be greatly enhanced by irradiation and thermal forces, might also be an important cause of ductilization. Further study is needed to understand the details of RIDU mechanisms in AM 316L.

Every stress-strain curve obtained at 500 and 600°C displayed serrated plastic flow over most of tested strain range, except for in the elastic and necking deformation ranges (Figures 17, 22, and 23). It is notable that such a serrated plastic flow or DSA effect [37,38] is commonly observed in all eight stress-strain curves, despite different initial microstructures and irradiation conditions. In the baseline testing, such serrated flow is observed to a much lesser degree in the tensile curves at 400°C. This is a phenomenon observed when some alloy elements—most likely Cr in austenitic SSs—move along with gliding dislocations, generating extra friction to the glides. As observed in the ductility data presented in Figure 6, the ductility reduction due to DSA is apparent in the range of ≥400°C in the 316L SSs. The DSA effect at lower temperatures (200–400°C) often causes significant ductility loss and fracture toughness in ferritic steels [51]. However, in the 316L SSs, the loss of ductility purely because of the DSA effect is insignificant because it occurs at high temperatures (≳400°C) in which dislocation locking by the affecting solute atoms cannot provide relatively weak resistance force. In addition, some portion of the serrations in the stress-strain curves is assumed to be contributed by the electrical noise of furnace heating operation, although no effort to detect and analyze such signals was performed in the project.

# 5. CURRENT STATUS OF IRRADIATION EXPERIMENT

## 5.1. Irradiation Experiments and Purposes

The TCR reactor includes many AM components made of primarily two metallic materials: AM 316L and AM Inconel (IN) 718 alloys. The metallic components of TCR fuel assembly will be AM with 316L SS powder and gas inlet and outlet structures with IN 718 alloy powder. Irradiation experiments and PIE were performed to provide materials performance data for assessing the AM metallic materials along with similar efforts for 3D printed SiC materials for the matrix and wall of fuel elements. The TCR irradiation and PIE campaign for 316L SSs includes irradiating 14 rabbit capsules in HFIR. The first six capsules were irradiated, and mechanical testing was performed for the specimens from four lower dose capsules in FY20 and FY21. Table 5 summarizes the irradiation plan and shows the target irradiation temperatures and doses of the 14 rabbit capsules and the tensile specimens loaded into these capsules. The irradiation campaigns for FY20 and FY21 intended to test different aspects and materials.

- The first six capsules (FY20) tested radiation effects on the AM 316L alloy in three different conditions (i.e., as-built, stress-relieved, and solution-annealed) and on the WT 316L reference alloy. Most of the PIE results from the 0.2 and 2 dpa capsules (GTCR01, GTCR02, GTCR04, and GTCR05) and the baseline test data for corresponding conditions are presented in the previous sections. PIE for the specimens irradiated to 8 dpa (from GTCR03 and GTCR06) is currently under preparation as the irradiation of those capsules was completed.
- The next four capsules (GTCR07–GTCR10 for FY21) include the AM 316L specimens taken from six different locations of 3D printed plates (Figure 26), which will test the effect of depth from the surfaces of 3D printed components. The six locations include the central layer of the 1.5 mm thick plate; the central and surface layers of the 5 mm thick plate; and the central, 10 mm deep, and surface layers of the 40 mm cube. Because the baseline testing for AM 316L materials in FY19 and the irradiation and PIE for FY20–21 led to the conclusion that AM 316L can perform best in the stress-relieved condition, the AM 316L specimens in this condition are irradiated in the ongoing and future irradiation campaign.
- The last four capsules (GTCR11–GTCR14 for FY21) are for the AM IN 718 alloy in four different heat-treatment conditions, which are the standard WT IN 718 alloy (i.e., solution-annealed and γ′- and γ″-aged conditions) and the AM IN 718 alloy in three different conditions (i.e., standard condition, solution-annealed condition, and solution-annealed at lowered temperature, as well as the γ′- and γ″-

aged conditions). Additional AM 316L specimens from different build locations are loaded in the spare spaces in these capsules.

**Table 5. Irradiation effect research and tensile specimens for metallic materials.**

| FY | Capsule ID | Target irradiation temp. (°C) | Dose (dpa) | Specimen/alloy |
|---|---|---|---|---|
| FY20 plan | GTCR01 | 300 | 0.2 | 36 SS-J2 (AM 316L in as-built, stress-relieved, and solution-annealed conditions and WT 316L) |
| | GTCR02 | 300 | 2 | 36 SS-J2 (AM 316L in as-built, stress-relieved, and solution-annealed conditions and WT 316L) |
| | GTCR03 | 300 | 8 | 36 SS-J2 (AM 316L in as-built, stress-relieved, and solution-annealed conditions and WT 316L) |
| | GTCR04 | 600 | 0.2 | 36 SS-J2 (AM 316L in as-built, stress-relieved, and solution-annealed conditions and WT 316L) |
| | GTCR05 | 600 | 2 | 36 SS-J2 (AM 316L in as-built, stress-relieved, and solution-annealed conditions and WT 316L) |
| | GTCR06 | 600 | 8 | 36 SS-J2 (AM 316L in as-built, stress-relieved, and solution-annealed conditions and WT 316L) |
| FY21 plan | GTCR07 | 300 | 2 | 24 SS-J3 (AM 316L in stress-relieved condition, six build locations) |
| | GTCR08 | 600 | 2 | 24 SS-J3 (AM 316L in stress-relieved condition, six build locations) |
| | GTCR09 | 300 | 10 | 24 SS-J3 (AM 316L in stress-relieved condition, six build locations) |
| | GTCR10 | 600 | 10 | 24 SS-J3 (AM 316L in stress-relieved condition, six build locations) |
| | GTCR11 | 300 | 2 | 24 SS-J2 (WT IN 718 in standard, one solution-annealed, and two age-hardened conditions, AM IN 718) and 8 SS-J3 (AM 316L in stress-relieved condition, six build locations) |
| | GTCR12 | 600 | 2 | 24 SS-J2 (WT IN 718 in standard, one solution-annealed, and two age-hardened conditions, AM IN 718) and 8 SS-J3 (AM 316L in stress-relieved condition, six build locations) |
| | GTCR13 | 300 | 10 | 24 SS-J2 (WT IN 718 in standard, one solution-annealed, and two age-hardened conditions, AM IN 718) and 8 SS-J3 (AM 316L in stress-relieved condition, six build locations) |
| | GTCR14 | 600 | 10 | 24 SS-J2 (WT IN 718 in standard, one solution-annealed, and two age-hardened conditions, AM IN 718) and 8 SS-J3 (AM 316L in stress-relieved condition, six build locations) |

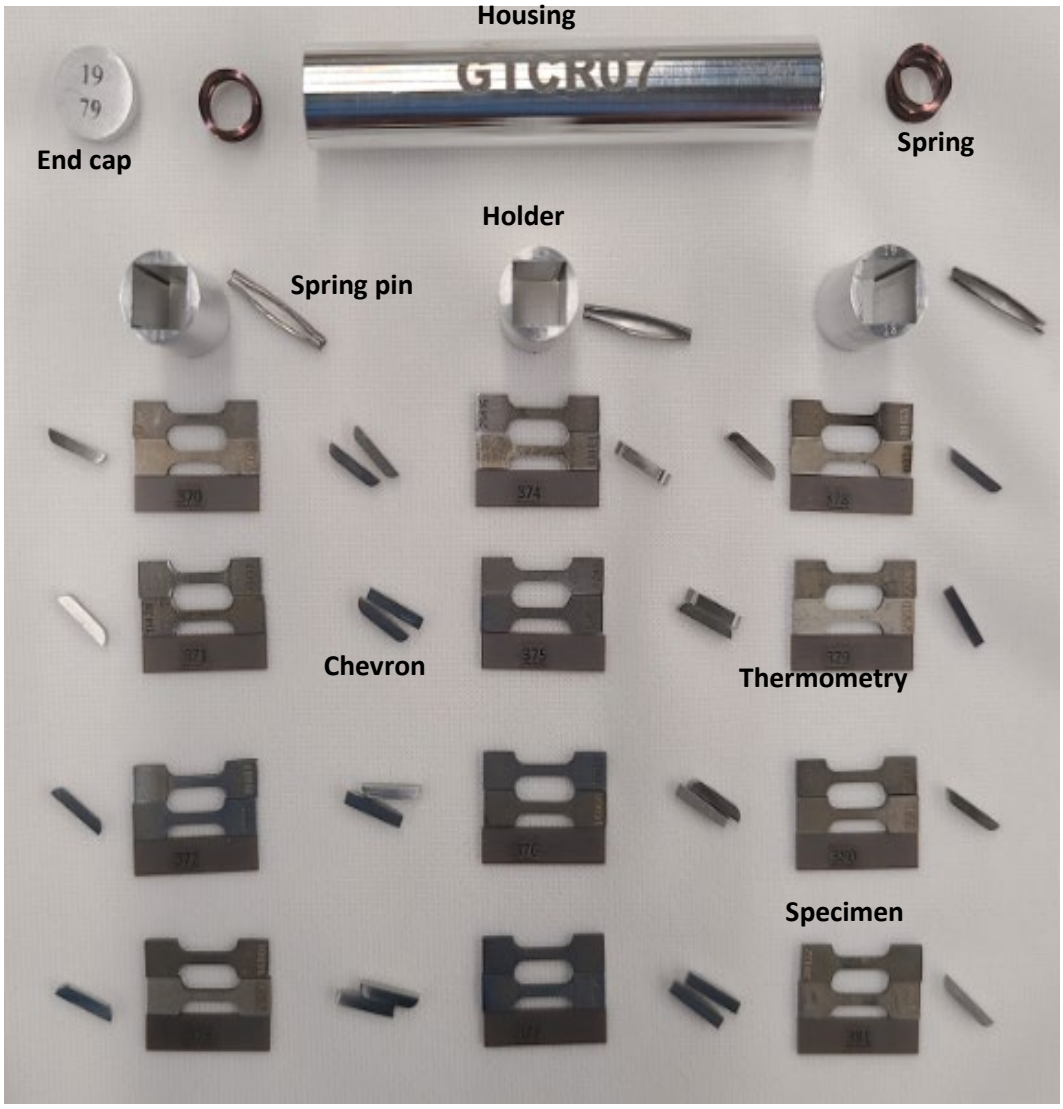


**Figure 26. A set of tensile specimens and capsule components to be assembled into one rabbit capsule (seen is the capsule GTRC07 for the irradiation of AM 316L).**

## 5.2. PIE Progress and Plans

The main PIE activities include uniaxial tensile testing to evaluate the mechanical performance of irradiated materials and electron microscopy to understand underlining mechanisms for the irradiation-induced microstructural and mechanical property changes. The first step of PIE activity is generally to disassemble capsules at ORNL's IMET facility, which is usually followed by specimen identification and sorting. Uniaxial tensile testing is performed by using the universal testing system at IMET. The microscopy samples, which are usually taken from tested tensile specimens or smaller pieces cut from them, and the passive thermometry samples are shipped to the LAMDA laboratory to perform detailed microscopy via TEMs or SEMs and to determine the average irradiation temperature of each capsule via the thermal dilatometry method. The current status and plan of PIE for the TCR program are summarized in Table 6.

**Table 6. Current status and plan for testing and evaluation after irradiation.**

| Capsule ID | Target irradiation temp. (°C) | Dose (dpa) | Irradiation | Status of PIE |
|---|---|---|---|---|
| GTCR01 | 300 | 0.2 | Completed | • Tensile tests at various temperature: completed<br>• Microscopy (TEM): ongoing |
| GTCR02 | 300 | 2 | Completed | • Tensile tests at various temperature: completed<br>• Microscopy (TEM): ongoing |
| GTCR03 | 300 | 8 | Completed | • Tensile tests at various temperature: being prepared<br>• Microscopy (TEM): planned |
| GTCR04 | 600 | 0.2 | Completed | • Tensile tests at various temperature: completed<br>• Microscopy (TEM): ongoing |
| GTCR05 | 600 | 2 | Completed | • Tensile tests at various temperature: completed<br>• Microscopy (TEM): ongoing |
| GTCR06 | 600 | 8 | Completed | • Tensile tests at various temperature: being prepared<br>• Microscopy (TEM): planned |
| GTCR07 | 300 | 2 | Completed | • Tensile testing and microscopy planned for FY22 |
| GTCR08 | 600 | 2 | Completed | • Tensile testing and microscopy planned for FY22 |
| GTCR09 | 300 | 10 | To be completed in FY22 | • Tensile testing and microscopy planned for FY22 |
| GTCR10 | 600 | 10 | To be completed in FY22 | • Tensile testing and microscopy planned for FY22 |
| GTCR11 | 300 | 2 | Completed | • Tensile testing and microscopy planned for FY22 and FY23, together with aging effect study |
| GTCR12 | 600 | 2 | Completed | • Tensile testing and microscopy planned for FY22 and FY23, together with aging effect study |
| GTCR13 | 300 | 10 | To be completed in FY22 | • Tensile testing and microscopy planned for FY22 and FY23, together with aging effect study |
| GTCR14 | 600 | 10 | To be completed in FY22 | • Tensile testing and microscopy planned for FY22 and FY23, together with aging effect study |

PIE tasks will be performed gradually as more irradiated samples become available in IMET and LAMDA. First, the TEM examination of the materials from capsules GTCR01, GTCR02, GTCR03, and GTCR06 will be started as soon as the samples are delivered to LAMDA lab, followed by tensile testing the 8 dpa specimens from the GTCR03 and GTCR06 capsules in FY22. Second, uniaxial tensile testing at selected temperatures (at least at RT and irradiation temperatures) and associated microscopy analysis will be performed for the specimens after irradiation to 2 dpa in capsules GTCR07, GTCR08, GTCR11, and GTCR12 throughout FY22. Third, PIE for the 10 dpa capsules GTCR09, GTCR10, GTCR13, and GTCR14 will be performed throughout FY22 and possibly during FY23. An aging effect study on the IN 718 alloy samples will be also performed for the same period.

## 6. SUMMARY AND CONCLUSION

The irradiation experiment and PIE efforts for accessing metallic materials focused on evaluating the mechanical performance of AM components over the TCR-relevant temperature range. Uniaxial tensile

testing was performed to evaluate the deformation behavior and mechanical properties of AM and reference WT 316L SSs before and after irradiation. Three AM 316L SSs in the as-built, stress-relieved (650°C/1 h), and solution-annealed (1,050°C/1 h) conditions and one reference 316L SS in WT (hot-rolled and solution-annealed) condition were prepared for the baseline and postirradiation testing.

The irradiation and PIE campaign for metallic materials includes irradiating 14 rabbit capsules up to 10 dpa in HFIR. Thus far, the irradiation of the first 10 capsules was completed, and the PIE for the miniature SS-J2 tensile specimens from four low-dose (0.2 and 2 dpa) capsules irradiated at target temperatures of 300 and 600°C was performed. In the PIE, uniaxial tensile tests were conducted in selected irradiation conditions only, including RT, 300°C (and 260°C and 390°C), 500°C, and 600°C.

The tensile testing results before and after HFIR irradiation are compared in this report, and the following conclusions were drawn.

- Regardless of the postbuild processing, the AM 316L SS before irradiation showed higher strength but relatively similar ductility compared with the reference 316L SS. Both the strength and the ductility of AM 316L and WT 316L SSs decreased with the test temperature.

- A significant effect of postbuild heat treatment was measured mostly in the low-strain region, and the effect became much smaller in the later part of deformation. Overall, the AM 316L SS demonstrated high strength and high ductility regardless of different postbuild heat treatments.

- Weibull plots of tensile property data indicated that in general larger variability was found in the ductility datasets than in the strength datasets. The tensile properties for the specimen sets from various build locations showed clear location dependence, although the measured variations were insignificant.

- Neutron irradiation induced significant changes in the mechanical behavior of AM SSs, including radiation-induced hardening and softening. Irradiation hardening was generally lower in the relatively stronger materials (i.e., the as-built and stress-relieved AM SSs) than in the solution-annealed AM and WT SSs.

- Relatively lower strength 316L SSs retained better ductility, regardless of irradiation conditions; however, the stronger 316L SSs demonstrated similar levels of ductility after the higher temperature (~600°C) irradiation. The as-built 316L steel after irradiation at 300°C showed unstable plastic deformation (i.e., necking) immediately after yielding, whereas the tensile property changes except the 300°C case were much less significant.

- No embrittlement (i.e., failure before yielding) was observed within the tensile test campaign or in the irradiation conditions explored in the experiment, which might be the key basis enabling to assess the AM 316L SSs for in-reactor applications.

- As a special phenomenon for high strength materials, the irradiation-induced ductilization behavior was observed after the higher temperature irradiation. Dynamic strain aging was also observed in the stress-strain curves obtained at high temperatures (≳400°C), regardless of irradiation dose; however, its negative effect is insignificant.

- Based on the baseline and postirradiation test results obtained so far, the stress-relieved AM 316L is considered the standard condition of AM 316L for the TCR core structure because it retains high strength without showing any risk of embrittlement (i.e., a complete loss of ductility) during service.

## 7. REFERENCES


[1] Steven J. Zinkle, Jeremy T. Busby, "Structural materials for fission & fusion energy," *Materials Today,* 12 (2009) 12-19.

[2] P.J. Maziasz and J. T. Busby, "Properties of Austenitic Steels for Nuclear Reactor Applications," *Comprehensive Nuclear Materials,* 2 (2012) 267–283.

[3] "Structural Materials for Liquid Metal Cooled Fast Reactor Fuel Assemblies-Operational Behavior," *IAEA Nuclear Energy Series, NF-T-4.2,* 2012.

[4] S. Sahin, M Übeyli, "A Review on the Potential Use of Austenitic Stainless Steels in Nuclear Fusion Reactors," *J. Fusion Energy,* 27 (2008) 271–277.

[5] A. A. Tavassoli, "Assessment of Austenitic Stainless Steels," *Fusion Engineering and Design,* 29 (1995) 371–390.

[6] V. Karthik, S. Murugan, P. Parameswaran, C. N. Venkiteswaran, K. A. Gopal, N. G. Muralidharan, S. Saroja, K. V. Kasiviswanathan, "Austenitic Stainless Steels for Fast Reactors -Irradiation Experiments, Property Evaluation and Microstructural Studies," *Energy Procedia,* 7 (2011) 257–263.

[7] "Austenitic Stainless Steels," in *Stainless Steels for Design Engineers*, ASM International, 2008.

[8] K.G. Field, J. Simpson, M. N. Gussev, H. Wang, M. Li, X. Zhang, X. Chen, T. Koyanagi, K. Kane, A. Marquez Rossy, M. Balooch, and K.A. Terrani, "Handbook of Advanced Manufactured Material Properties from TCR Structure Builds at ORNL – FY19," ORNL/TM-2019/1328, Oak Ridge National Laboratory, 2019.

[9] J. Simpson, J. Haley, C. Cramer, O. Shafer, A. Eilliott, W. Peter, L. Love, R. Dehoff, "Considerations for Application of Aadditive Manufacturing to Nuclear Reactor Core Components," ORNL/TM-2019-1190, Oak Ridge National Laboratory, 2019.

[10] T. S. Byun, M. N. Gussev, T. G. Lach, M. R. McAlister, J. J. Simpson, B. E. Garrison, Y. Yamamoto, C. B. Joslin, J. K. Carver, F. A. List, R. R. Dehoff, K. A. Terrani, M. Li, X. Zhang, "Mechanical Properties and Deformation Behavior of Additively Manufactured 316L Stainless Steel – FY 2020," ORNL/TM-2020/1574, Oak Rodge Nationalaboratory, 2020.

[11] T.S. Byun, B.E. Garrison, M.R. McAlister, X. Chen, M.N. Gussev, T.G. Lach, A. Le Coq, K. Linton, et al., "Mechanical behavior of additively manufactured and wrought 316L stainless steels before and after neutron irradiation," *J. Nucl. Mater.,* 548 (2021) 152849.

[12] B. M. Morrow, T. J. Lienert, C. M. Knapp, J. O. Sutton, M. J. Brand, R. M. Pacheco, V. Livescu, J. S. Carpenter, G. T. Gray, "Impact of Defects in Powder Feedstock Materials on Microstructure of 304L and 316L Stainless Steel Produced by Additive Manufacturing," *Metall. Mater. Trans. A,* 49 (2018) 3637–3650.

[13] T. Ronneberg, C. M. Davies, and P. A. Hooper, "Revealing Relationships between Porosity, Microstructure and Mechanical Properties of Laser Powder Bed Fusion 316L Stainless Steel through Heat Treatment," *Mater. Des.,* 189 (2020) 108481.

[14] A. J. Birnbaum, J. C. Steuben, E. J. Barrick, A. P. Iliopoulos, J. G. Michopoulos, "Intrinsic Strain Aging, Σ3 Boundaries, and Origins of Cellular Substructure in Additively Manufactured 316L," *Addit. Manuf.,* 29 (2019) 100784.

[15] U. S. Bertoli, B .E. MacDonald, J. M. Schoenung, "Stability of Cellular Microstructure in Laser Powder Bed Fusion of 316L Stainless Steel," *Mater. Sci. Eng. A,* 739 (2019) 109–117.

[16] M. Li, X. Zhang, W.Y. Chen, F. Heidet, "Progress Report on the Assessment of the Material Performance for TCR Applications," ANL/NSE-20/12, Argonne National Laboratory, 2020.

[17] T. Kurzynowski, K. Gruber, W. Stopyra, B. Kuźnicka, E. Chlebus, "Correlation between Process Parameters, Microstructure and Properties of 316 L Stainless Steel Processed by Selective Laser Melting," *Mater. Sci. Eng. A,* 718 (2018) 64–73.

[18] C. R. Brinkman, "Elevated-Temperature Mechanical Properties of an Advanced Type 316 Stainless Steel, United States," ORNL/CP-101053, Oak Ridge National Laboratory, 1999.

[19] E. Garlea, H. Choo, C. C. Sluss, M. R. Koehler, R. L. Bridges, X. Xiao, Y. Ren, B. H. Jared, "Variation of Elastic Mechanical Properties with Texture, Porosity, and Defect Characteristics in Laser Powder Bed Fusion 316L Stainless Steel," *Mater. Sci. Eng. A,* 763 (2019) 138032.

[20] T. Pinomaa, M. Lindroos, M. Walbrühl, N. Provatas, A. Laukkanen, "The Significance of Spatial Length Scales and Solute Segregation in Strengthening Rapid Solidification Microstructures of 316L Stainless Steel," *Acta Mater.,* 184 (2020) 1–16.

[21] M. Li, X. Zhang, W.Y. Chen, F. Heidet, T. S. Byun, K.A. Terrani, "Creep Behavior of 316L Stainless Steel Manufactured by Laser Powder Bed Fusion," *J. Nucl. Mater.,* 548 (2021) 152847.

[22] D. Kong, X. Ni, C. Dong, L. Zhang, C. Man, X. Cheng, and X. Li, "Anisotropy in the Microstructure and Mechanical Property for the Bulk and Porous 316L Stainless Steel Fabricated via Selective Laser Melting," *Mater. Lett. ,* 235 (2019) 1–5.

[23] J. Lin, F. Chen, X. Tang, J. Liu, S. Shen, and G. Ge, "Radiation-Induced Swelling and Hardening of 316L Stainless Steel Fabricated by Selected Laser Melting," *Vacuum,* 174 (2020) 109183.

[24] M. Song, M. Wang, X. Lou, R. B. Rebak, and G. S. Was, "Radiation Damage and Irradiation-Assisted Stress Corrosion Cracking of Additively Manufactured 316L Stainless Steels," *J. Nucl. Mater.,* 513 (2019) 33–44.

[25] G. Meric de Bellefon, K.M. Bertsch, M.R. Chancey, Y.Q. Wang, D.J. Thoma, "Influence of solidification structures on radiation-induced swelling in an additively-manufactured austenitic stainless steel," *J. Nucl. Mater.,* 523 (2019) 291-298.

[26] K.A. Terrani, T.G. Lach, H. Wang, A. Le Coq, K. Linton, C. Petrie, T. Koyanagi, T.S. Byun, "Irradiation stability and thermomechanical properties of 3D-printed SiC," *J. Nucl. Mater.,* 551 (2021) 152980.

[27] N. Suutala, T. Takalo, T. Moisio, "Ferritic-austenitic solidification mode in austenitic stainless steel welds," *Metall Mater Trans A,* 11 (1980) 717–725.

[28] P. Champlin, J. Burns, C. Petrie, X. Hu, K. D. Linton, R. Howard, K. A. Terrani, "Capsule and Specimen Geometries for HFIR Irradiation Testing Supporting the Transformational Challenge Reactor," ORNL/TM-2019/1310, Oak Ridge National Laboratory, 2019.

[29] A. G. Le Coq, K. D. Linton, P. Champlin, R. H. Howard, X. Hu, T. S. Byun, K. A. Terrani, "HFIR Irradiation Testing Supporting the Transformational Challenge Reactor," ANS Trans. (2020) 242–245.

[30] K. Farrell, T. S. Byun, "Tensile properties of candidate SNS target container materials after proton and neutron irradiation in the LANSCE accelerator," *J. of Nucl. Mater.,* 296 (1-3) (2001) 129–138.

[31] ASTM E8 / E8M, Standard Test Methods for Tension Testing of Metallic Materials, ASTM International, 2016.

[32] ASTM E21, Standard Test Methods for Elevated Temperature Tension Tests of Metallic Materials, ASTM International, 2020.

[33] Y.M. Wang, T. Voisin, J.T. McKeown, J. Ye, N. P. Calta, Z. Li, Z. Zeng, Y. Zhang, W. Chen, T. T. Roehling, R. T. Ott, M. K. Santala, P. J. Depond, M. J. Matthews, A. V. Hamza, T. Zhu, "Additively Manufactured Hierarchical Stainless Steels with High Strength and Ductility," *Nat. Mater.,* 17 (2018) 63–71.

[34] S. Li, J. Hu, W.-Y. Chen, J. Yu, M. Li, and Y. Wang, "Evolution of Cellular Dislocation Structures and Defects in Additively Manufactured Austenitic Stainless Steel under Ion Irradiation," *Scr. Mater. ,* 178 (2020) 245–250.

[35] Y. Zhong, L. Liu, S. Wikman, D. Cui, and Z. Shen, "Intragranular Cellular Segregation Network Structure Strengthening 316L Stainless Steel Prepared by Selective Laser Melting," *J. Nucl. Mater.,* 470 (2016) 170–178.

[36] Shilei Li, Jing Hu, Wei-Ying Chen, Jingyue Yu, Meimei Li, Yandong Wang,, "Evolution of cellular dislocation structures and defects in additively manufactured austenitic stainless steel under ion irradiation," *Scripta Mater.,* 178 (2020) 245-250.

[37] B. R. Antoun, C. Alleman, K. De La Trinidad, "Experimental Investigation of Dynamic Strain Aging in 304L Stainless Steel," SAND2018-3171C, Sandia National Laboratory, 2018.

[38] S. N. Monteiroa, F. M. Margem, V. S. Candido, A. Ben-Hur da Silva Figueiredo, "High Temperature Plastic Instability and Dynamic Strain Aging in the Tensile Behavior of AISI 316 Stainless Steel," *Materials Research,* 20 (2017) 506–511.

[39] W. Weibull, "A statistical distribution function of wide applicability,," *J. of Applied Mech. ,* 18 (3) (1951) 293–297.

[40] D.L. Naik, T. H. Fronk, "Weibull Distribution Analysis of the Tensile Strength of the Kenaf Bast Fiber," *Fibers and Polymers ,* 17 (2016) 1696-1701.

[41] K. Wallin, T. Saario, K. Törrönen, "Statistical model for carbide induced brittle fracture in steel," *Metal Science,* 18 (1984) 13–16.

[42] J. H. Yoon, T. S. Byun, J. P. Strizak, L. L. Snead, "Characterization of tensile strength and fracture toughness of nuclear graphite NBG-18 using subsize specimens," *J. Nucl. Mater.,* 2011 (412) 315–320.

[43] Y. Kitsunai, H. Kurishita, T. Kuwabara, M. Narui, M. Hasegawa, T. Takida, K. Takebe, "Radiation embrittlement behavior of fine-grained molybdenum alloy with 0.2 wt¾TiC addition," *J. Nucl. Mater.,* 346 (2005) 233- 243.

[44] D.J. Edwards, E.P. Simonen, S.M. Bruemmer, "Evolution of fine-scale defects in stainless steels neutron-irradiated at 275 C," *J. Nucl. Mater.,* 317 (2003) 13–31.

[45] R. E. Schramm, R. P. Reed, "Stacking Fault Energies of Seven Commercial Austenitic Stainless Steels," *Metall. Trans. A,* 6A (1975) 1345–1351.

[46] J. Talonen, H. Hänninen, "Formation of shear bands and strain-induced martensite during plastic deformation of metastable austenitic stainless steels," *Acta Mater.,* 55 (2007) 6108–6118.

[47] T. S. Byun, "On the Stress Dependence of Partial Dislocation Separation and Deformation Microstructure in Austenitic Stainless Steels," *Acta Mater.,* 51 (2003) 3063–3071.

[48] T. S. Byun, N. Hashimoto, K. Farrell, "Temperature Dependence of Strain Hardening and Plastic Instability Behaviors in Austenitic Stainless Steels," *Acta Mater.,* 52 (2004) 3889–3899.

[49] T. S. Byun, N. Hashimoto, K. Farrell, "Deformation Mode Map of Irradiated 316 Stainless Steel in True Stress-Dose Space," *J. Nucl. Mater.,* 351 (2006) 303–315..

[50] A. Hishinuma, K. Fukai, T. Sawai, K. Nakata, "Ductilization of TiAl intermetallic alloys by neutron-irradiation," *Intermetallics,* pp. 4 (1996) 179-184.

[51] G. C. Soares, R. R. U. Queiroz, L. A. Santos , "Effects of Dynamic Strain Aging on Strain Hardening Behavior, Dislocation Substructure, and Fracture Morphology in a Ferritic Stainless Steel," *Metall. Mater. Trans. A,* 51 (2020) 725–739.